

Late Holocene current patterns in the northern Patagonian fjords recorded by sediment drifts in Aysén Fjord

Katleen Wils^a, Marlies Wermersche^a, David Van Rooij^a, Galderic Lastras^b, Frank Lamy^c, Helge W. Arz^d, Giuseppe Siani^e, Sebastien Bertrand^a, and Maarten Van Daele^a

^a*Renard Centre of Marine Geology (RCMG), Department of Geology, Ghent University, Ghent, Belgium*

^b*GRC Geociències Marines, Universitat de Barcelona, Barcelona, Spain*

^c*Alfred Wegener Institut für Polar- und Meeresforschung, Bremerhaven, Germany*

^d*Leibniz Institute for Baltic Sea Research Warnemünde (IOW), Rostock-Warnemünde, Germany*

^e*GEOPS, UMR 8148 Université de Paris-Saclay, Orsay, France*

Corresponding author: Katleen Wils (katleen.wils@ugent.be)

Abstract

Present-day circulation patterns in the southeastern Pacific Ocean are driven by the Antarctic Circumpolar Current, directing subantarctic surface water into the Patagonian fjords since at least the early Holocene. In this way, bottom current patterns in the area are regulated by the regional climate, although the complex bathymetry of the fjords has a significant impact as well. To understand the potential interplay of climate, seafloor topography and circulation patterns, we study the sedimentary infill of Aysén Fjord (~45°S) and reveal the first active sediment drifts in the region. These allow constraining the present-day circulation patterns in northern Patagonia and show an incoming (southward) as well as returning (northward) flow direction. While the general sedimentary evolution of the fjord (and thus also the sediment drifts) is climate-driven (i.e., it reflects variability in southern westerly wind strength), the onset of drift formation at ~3.7 ka does not seem to have originated from an abrupt change in regional climate. Instead, we propose that a megathrust earthquake described in paleoseismic records in the area could have resulted in subsidence of one (or more) of the many

bathymetric highs in the Patagonian fjords, thus contributing to enhanced spilling of subantarctic water into the fjord. This study underscores the importance of multidisciplinary research to understand past and present bottom current circulation patterns and disentangle different possible feedback mechanisms.

Keywords

Patagonia, sediment drift, bottom current circulation, climatic variability, tectonic control

1 Introduction

The present-day oceanic surface circulation pattern near the west coast of southern South America is dominated by the northern margin of the Antarctic Circumpolar Current (ACC), carrying cold, relatively fresh and nutrient-rich subantarctic water to the Chilean coastline (Strub et al., 1998). The ACC is considered to be mostly wind-driven, depending on the belt of westerly winds between 45 and 55°S (Barker and Thomas, 2004). These Southern Westerly Winds (SWW) also largely determine the existing climate patterns in southern South America, characterized by drastically stronger precipitation on the western side of the Andes compared to the eastern flank (Garreaud et al., 2013). Consequently, numerous studies have aimed at reconstructing the late glacial and Holocene climate evolution of the southern mid-latitudes by revealing variability in the strength and position of the westerlies and/or ACC through time (e.g., Haddam et al., 2018; Heirman et al., 2012; Kilian and Lamy, 2012; Lamy et al., 2010; Lamy et al., 2002; Moreno et al., 2010; Romero et al., 2006; Saunders et al., 2018; Verleye and Louwye, 2010; Villa-Martínez and Moreno, 2007). Many of these studies have focussed on the Chilean margin and Patagonia, forming the only major landmass intersecting the SWW.

A large portion of Chilean Patagonia consists of channels and fjords, forming one of the largest estuarine systems in the world. These are in direct connection with the open ocean, resulting in a permanent inflow of subpolar as well as (deeper) subtropical water masses that currently dominate the oceanic realm in the area (Palma and Silva, 2004). The morphology of these channels is rather

complex, shaped through a variety of tectonic and glaciological processes (e.g., Bianchi et al., 2020; Glasser and Ghiglione, 2009; Syvitski et al., 1987). As a result, circulation patterns in the region are land-constrained, overprinting the climate-driven oceanic current dynamics. This significantly complicates the regional feedback mechanisms between bottom currents and climate, of which the evolution through time remains largely unknown. The study of sediment drifts provides a potential way forward in unravelling the missing link between these factors, as formation and evolution of such sedimentary structures is related to bottom current activity (Rebesco et al., 2014) and can result from climate changes (e.g., Amblas et al., 2006; Gilli et al., 2004; Grützner et al., 2005; Heirman et al., 2012; Van Daele et al., 2016) as well as tectonic activity (e.g., García et al., 2009; Lobo et al., 2011; Roque et al., 2012). However, the study of sediment drifts in the Patagonian fjords was, up to now, limited to identification of an ancient drift in Reloncaví Fjord (~42°S, St-Onge et al., 2012).

This study presents a geophysical and sedimentological analysis of the sedimentary infill of the outer part of Aysén Fjord (~45°S), which allows documenting the first sediment drifts in the region, with the aim of reconstructing the post-glacial evolution of bottom currents in the Chilean Patagonian fjords. More specifically, as Aysén Fjord is shielded from the influence of any deep-water masses by the presence of a bathymetric high resulting in < 50 m water depth (Sievers and Silva, 2008), it forms an ideal location to isolate the surficial subantarctic water mass and demonstrate its evolution in the region, which can potentially be related to climatic as well as tectonic variability.

2 Regional setting

2.1 Oceanographic and hydrographic setting

The Pacific Patagonian coastline is characterized by numerous channels and fjords (Fig. 1A), formed as a result of glacial action and tectonic processes during Cenozoic times (e.g., Glasser and Ghiglione, 2009; Syvitski et al., 1987). Aysén Fjord is one of them, with a length of over 70 km, connecting the Aysén River and its catchment in the east to the Costa Channel on its western extremity (Fig. 1B). Just north of Aysén Fjord, the Costa Channel merges with the Errázuriz Channel into the Moraleda Channel.

The latter communicates with the Pacific Ocean through the Boca del Guafo (~43.5°S), located south of Chiloé Island, and almost 200 km north of Aysén Fjord. Due to the limited depth of these channels (~70-400 m), only the surficial water masses present in the open ocean can enter the Patagonian channels and fjords (Fig. 1C), including the Subantarctic Water (SAAW, up to 150 m depth) and the Equatorial Subsurface Water (ESSW, 150-300 m depth) (Sievers and Silva, 2008; Silva and Guzmán, 2006). The SAAW is under direct influence of the ACC (Fig. 1A), currently hitting the South American continent between around 40°S and 45°S, where it splits into a southward and northward current, respectively the Cape Horn Current and Humboldt Current (e.g., Strub et al., 1998). The Cape Horn current pushes the SAAW into the Moraleda Channel through the Boca Del Guafo, where it becomes mixed with a surface layer of fresh water originating from rivers, coastal runoff, glacial melting and precipitation. This results in the formation of two separate water masses, termed the Modified Subantarctic Water (MSAAW) and a surficial, less saline layer about 50 m thick referred to as Estuarine Water (EW) (Sievers and Silva, 2008; Silva and Guzmán, 2006). The MSAAW can flow as far as ~46.5°S, thus also entering Aysén Fjord, where it is blocked by the shallowing bathymetry (Sievers and Silva, 2008). The deeper ESSW, on the other hand, is blocked further north by the presence of several topographic highs on the rather irregular ocean floor, most importantly the Meninea sill, just north of Aysén Fjord (Fig. 1C).

Apart from controlling the surficial oceanic circulation patterns in the southern Pacific, the ACC also plays an essential role in the regional and even global climate (e.g., Barker and Thomas, 2004; Kilian and Lamy, 2012; Rintoul, 2018; Sijp and England, 2008). Its location is strongly coupled to the latitude of the SWW belt and can extend up to 10° more northward during glacial periods (e.g., Kaiser et al., 2005; Lamy et al., 2004; Verleye and Louwye, 2010). Such changes in position as well as strength of the SWW are reflected in the regional precipitation patterns west of the Andes, where the amount of precipitation is positively correlated to wind velocities (e.g., Garreaud et al., 2013; Lamy et al., 2010). Present-day annual precipitation can be as high as 10,000 mm at around 50°S but fluctuates between 600 and 2,200 mm in the Aysén River watershed, and reaches up to 2,500 mm along the fjord (Fick and

Hijmans, 2017). This results in voluminous pluvio-nival rivers feeding the fjord, the largest of which is Aysén River (Fig. 1B) with an average discharge of 521 m³/sec (Calvete and Sobarzo, 2011). River discharge modulates the thickness of the EW (Calvete and Sobarzo, 2011) and constitutes the main source of sediment to the fjord, which is almost entirely deposited through settling from the EW (Bertrand et al., 2012). Glaciers are currently absent from the Aysén watershed. They started retreating to their present extent after the Last Glacial Maximum (LGM, ~60 to 18 cal ka BP) in response to an initial warming period that lasted up to ~15 cal ka BP, followed by a plateau and a second temperature rise around 12.5 cal ka BP (Davies et al., 2020; Haddam et al., 2018; Kilian and Lamy, 2012).

2.2 Seismic and volcanic activity

Southern Chile is a tectonically active region, located along the southern section of the Peru-Chile subduction trench (Fig. 1B) where the Nazca plate converges with the South American Plate (Fisher and Raitt, 1962). This results in oblique subduction, of which the trench-parallel component is accommodated by the presence of an active dextral strike-slip lineament, the Liquiñe-Ofqui Fault Zone (LOFZ), located along-strike of the subduction zone (Cembrano et al., 1996). Aysén Fjord is located on the LOFZ, about 200 kilometres from the subduction zone (Fig. 1B). The last significant earthquake (M_w 6.2) along the LOFZ occurred in April 2007 and had its epicentre located in the inner part of Aysén Fjord (Legrand et al., 2011), triggering multiple landslides in its catchment (Sepúlveda et al., 2010). The sedimentary infill of the fjord revealed that similar crustal earthquakes have occurred throughout the Holocene (Wils et al., 2018), and even shaking related to past megathrust earthquakes has affected the fjord (Wils et al., 2020). Another direct consequence of the subduction zone is the presence of a volcanic chain with mostly tholeiitic and high-Al basalts as well as basaltic andesites (Stern, 2004). The main volcanoes in the vicinity of Aysén Fjord are the Mentolat, Cay, Macá, and Hudson Volcano (Fig. 1B). The only known eruptions for Mentolat and Macá Volcano occurred ~7,500 and ~1,400 cal yrs BP, respectively, while no records of Holocene activity exist for Cay Volcano (Naranjo and Stern, 2004). Hudson Volcano has had multiple major eruptions during the Holocene, including the H1 (~8,200 cal yrs BP) and H2 (~3,900 cal yrs BP) eruptions and several other smaller activity (Naranjo and Stern, 1998;

Stern and Weller, 2012). Although tephra deposits related to these eruptions have been identified within the sedimentary infill of Aysén Fjord (Wils et al., 2018), volcanic fallout in the Patagonian fjords is generally limited due to the western-blowing SWW (Fontijn et al., 2014).

3 Material and methods

3.1 Bathymetry data

Multibeam data was recorded in March 2013 during the DETSUFA cruise on board *BIO Hespérides* (Lastras and The Shipboard Scientific Party, 2013). An EM 1002S Kongsberg multibeam echosounder was used, providing high-resolution bathymetric data in the entire fjord (Fig. 2). The system operated with an equidistant beam spacing, using a nominal sonar frequency of 95 kHz and 111 beams of 2x2° per ping. Swath width was set to 300 m, resulting in a footprint of about 3 m (Lastras and The Shipboard Scientific Party, 2013). After processing, the resulting bathymetry map was imported in IHS Kingdom Suite software for integration with the seismic reflection profiles.

To complement the multibeam data, which does not cover the entire outer fjord area, the GEBCO 2020 bathymetry grid was used, which has a 450 m resolution (GEBCO Compilation Group, 2020).

3.2 Seismic reflection profiles

Reflection-seismic profiles were also acquired during the DETSUFA cruise, resulting in a dense network of long, (mostly) fjord-parallel lines (Fig. 2A). A Kongsberg TOPAS PS18 parametric subbottom profiler was used, operating at a secondary central frequency of 1.5-4.5 kHz (Lastras and The Shipboard Scientific Party, 2013). This resulted in a theoretical vertical resolution of about 0.2 ms two-way travel time (TWT), which corresponds to ~15 cm. Real-time processing of the seismic data was performed on board of the *BIO Hespérides*, after which the data was imported in the IHS Kingdom Suite software for visualization and interpretation. Seismic-stratigraphic units were distinguished based on visible changes in acoustic reflection and spatial distribution.

3.3 Sedimentological analyses

Two Calypso sediment cores (MD07-3114 and MD07-3115, Fig. 2) were taken in the outer fjord during the PACHIDERME survey in February 2007 on board *RV Marion-Dufresne* (Kissel et al., 2007). Based on preliminary on-board interpretations of the seismic data, these cores were retrieved with the intention of having a partly overlapping sedimentary sequence. Both cores have a length of just under 32 metres, and were split and described immediately after retrieval, after which they were scanned at a 2 cm interval using the on-board multi-sensor core logger to reveal, among others, their gamma density and magnetic susceptibility (MS).

Grain-size distributions were measured on 1 cm-thick slices using a Malvern Mastersizer 3000. A sampling resolution of 20 cm was applied throughout core MD07-3114 and increased to 10 or even 5 cm in specific areas of interest. Only the first 3.5 m of core MD07-3115 (i.e. the part that overlaps with core MD07-3114 based on preliminary correlation, Kissel et al. (2007)) were sampled for grain-size analysis, with samples retrieved every 4 cm (when possible). The terrigenous sediment fraction was isolated by chemical pre-treatment with H₂O₂ (2 ml, 30%), HCl (1 ml, 10%) and NaOH (1 ml, 2 N) to remove organic matter, carbonates and biogenic silica, respectively. Grains with a diameter larger than 1 mm were excluded for analysis by sieving. All samples were boiled with a sodium hexametaphosphate solution (1 ml, 2%) prior to analysis to ensure complete disaggregation. The geometric mean grain size and sorting values for the total grain-size distributions and sortable silt (SS) fractions (10–63 µm, McCave et al., 1995) were calculated using the GRADISTAT software (Blott and Pye, 2001).

Glass shards in two tephra layers at 15.9 m depth in core MD07-3114 and 2.24 m in core MD07-3115 have been analysed for their major-element composition using a CAMECA-SX 100 Electron Microprobe (EPMA-CAMPARIS) at the Université Paris VI in France following the procedure by Carel et al. (2011). Ten elements were analysed (Na, Mg, Si, Al, Cl, K, Ca, Ti, Mn, and Fe) using an accelerating voltage of 15 KV, a current of 10 nA and a beam size of 5 µm to minimize loss of alkalis such as Na. Precisions on

individual shards (1σ) were better than 0.6% for Si, ~1% for Al, 3% for Ca and Mg, 4% for Na, 5% for Fe, 6% for K, 10% for Ti, and about 30% for Cl and Mn.

Radiocarbon ages for selected depths in both cores have been obtained by Serno (2009) using a combination of plant remains and shells (Table 1). The occasional occurrence of shells and plant debris is most common in core MD07-3114. Here, we recalibrate all these radiocarbon ages using the more recent SHCal20 calibration curve (Hogg et al., 2020) and combine them into a single age-depth model for both cores using the Bacon R-package (Blaauw and Christen, 2011). A reservoir age of 550 years is considered for the marine samples (Serno, 2009), to which we add an uncertainty of 40 years—corresponding to the average error on the radiocarbon ages themselves.

4 Results

4.1 Seismic stratigraphy and bathymetric description

The seismic profiles allow defining six acoustic units that overly the acoustic basement—below which only locally unclear reflectors are observed—and are numbered in order of deposition (1, 2, 3, 4). The oldest of these units (Unit 0) consists of a succession of mostly parallel low- and high-amplitude reflections. This thick unit can only be identified in the deepest parts of the basin, where seismic penetration is limited, and hence, the base of this unit cannot be observed. Its distribution is bounded by the steep bedrock slopes associated to the mainland and/or some of the islands in the fjord (Casma, Churrecue and Elena Island, Fig. 2A). This is also true for Unit 1, a relatively thin, ponding unit with a largely acoustically transparent seismic facies near the western extent of the fjord, gradually becoming more stratified towards the inner fjord. Unit 2 consists of a succession of closely-spaced parallel high-amplitude reflections, filling up the deepest part of the basin. As a result, Unit 3 extends further towards the inner fjord but remains bounded by the subaquatic continuation of Churrecue and Elena Island. Several parallel high-amplitude reflections can be identified, albeit with a more pronounced alternation with lower-amplitude reflections compared to Unit 2. Unit 4 can be identified

throughout most of the outer part of the fjord, consisting of a seismic facies with parallel, low-amplitude reflections and a single strong horizon in the lower half. With the exception of slight sediment thickening south of core MD07-3115 (Fig. 4), giving the unit a subtle mounded nature, variations in sediment thickness are mostly restrained by the irregular bedrock topography, as is the case for the older sedimentation in the fjord. The most recent seismic unit (Unit 5) consists of mostly low-amplitude reflections and covers the entire outer part of Aysén Fjord, with the presence of a single, basin-wide high-amplitude reflection (Figs. 3, 4). In the centre of the basin, this unit is mostly subparallel stratified. Unit 5 has a similar seismic facies compared to Unit 4, however, several mounded morphologies are present showing a gradual thinning of the reflectors mostly towards the basin periphery (e.g., , 4). In contrast to the units below, Unit 5 thus shows strong thickness variability that results in several mounded areas and local depressions with a relief of 30 m or more. This includes the mounded area in which core MD07-3114 was retrieved, which covers about 6.5 km² and is bounded in the west by an elongated, roughly north-south oriented depression of similar extent visible in the present-day bathymetry (Fig. 2B). This depression stretches from the location of core MD07-3115 to the southern limit of the fjord (into the Costa Channel), but is less pronounced in the central part of the basin (Fig. 2B, Fig. 4). In this central part, the transition from the depression to the mounded area is punctuated by a subsurface fault (Fig. 2B, Fig. 4). Another major mounded sediment package of over 20 m thick is present in the central part of the outer fjord basin (~13 km²), confined between the north-south oriented depression in the east and a series of small (<0.5 km²), individual depressions with a comma-like shape towards the western extremity of the fjord, close to Casma Island (Fig. 2C). These latter depressions are much steeper and narrower compared to the central depression (Fig. 2B), and older sedimentation (Units 3 and/or 4) is occasionally eroded here (Fig. 4). A more pronounced case of erosion can be observed in the elongated east-west oriented depression of about 4 km long and 1.5 km wide just northwest of the coring locations along the shoreline of Churrecue Island (Fig. 2A). This

forms an erosive channel-like structure that seems to prevent deposition of recent sediments and in which erosion occurred down to the base of Unit 3 ().

4.2 Sedimentological characterization

Both sediment cores have a mostly light-coloured greyish fine-grained appearance and are bioturbated throughout. Core MD07-3114 is located in an area where Unit 5 is relatively thick (mounded), whereas MD07-3115 is retrieved in one of the depressions where the recent sedimentation is more condensed (). Therefore, core MD07-3114 allows visualizing the recent sedimentation in great detail, while MD07-3115 provides a window to the older sedimentation in this part of the fjord.

The lower 5 m of sediments in core MD07-3115 consists of predominantly siliciclastic sediments with a very low diatom content, including marine, brackish and freshwater species (Kissel et al., 2007). Additionally, this sediment package shows strong fluctuations in MS and density (Fig. 5) consisting of a sharp rise at their base followed by a gradual decrease. Each of these peaks corresponds to a dark, visually coarser-grained layer. These darker beds show a sharp basal contact and are generally laminated. Considering that density contrasts form the base for changes in acoustic impedance, these layers are considered as the sediment beds that are responsible for the closely-spaced high-amplitude reflections in Unit 2 (Fig. 3). Sedimentation remains siliciclastic up to about 19.5 m core depth, showing similar dark sediment beds characterized by strong fluctuation in MS and density, although they are less numerous here (Fig. 5). We therefore interpret that these high-density beds correspond to the less-closely spaced strong reflectors in Unit 3.

At around 19.5 m depth in MD07-3115, the lithology abruptly changes from dominantly siliciclastic to diatom-rich clays. Up to about 7 m, sediments are also lighter-coloured compared to the sediments below. MS and density reach their lowest values in this interval and start increasing from about 14 m depth (Fig. 5). At about 13 m, a tephra layer is present resulting in a sharp peak in MS and density that

we correlate to the strong reflector present in the lower part of Unit 4. Similar light-coloured diatom-rich clays can be identified in the lowermost part of core MD07-3114, hinting towards a first part of overlap between both sediment cores. This overlap is confirmed by a darker-coloured sediment interval that can be identified on top of the light-coloured sediments in both cores (between 7 and 4.5 m in MD07-3115 and 31 to 28 m in MD07-3114), marked by two well-defined, quasi-identical increases in MS that coincide with slight mean grain-size increases visible in MD07-3114 (Fig. 5). On top of this darker-coloured sediment interval, sedimentation resumes to its previous lighter colours and shows another, considerably smaller, MS peak. Up to here, sedimentation is thus roughly consistent in both core locations and no noteworthy lateral thickness variations occur. This is no longer the case for the most recent sedimentation in both cores, as marked by their clearly deviating trends in MS (Fig. 5). Therefore, we consider this boundary to mark the base of Unit 5, where sediment thinning results in the upper ~27 m of sediment in core MD07-3114 to be condensed into the upper ~3 m of sediment in core MD07-3115 ().

Sedimentation in Unit 5 is again lighter in colour and remains diatom-rich. Similar to the seismic facies, there is no visual change in sedimentary facies between Unit 4 and Unit 5 (, Fig. 4). Nevertheless, the base of Unit 5 is marked by an abrupt increase in SS mean grain size in both cores, after which SS mean grain size shows an overall gradual decrease, albeit divided in two steps (Fig. 5). The transition between the two steps (~13 m in MD07-3114, ~2 m in MD07-3115) is marked by a through in SS mean grain size. Despite these similar trends in both core locations, SS values are markedly higher in MD07-3115 (where Unit 5 is more condensed) compared to MD07-3114—a trend that is also reflected in the mean grain size. This underscores the lateral variability in sedimentation, supported by the remaining sedimentary parameters; MS, density and mean grain size roughly follow the same trend as the SS at the location of MD07-3115, while these parameters remain rather stable

in core MD07-3114 (Fig. 5). Only the upper 4 m of sediment in core MD07-3114 show an increasing trend in MS and density values.

A coarse-grained tephra layer can be identified at both core locations, resulting in a sharp MS peak as well as an increase in mean grain size (after sieving and removal of grains with a diameter > 1 mm) that is not reflected in the SS. This tephra layer is present at about 16 m depth in core MD07-3114 and at 2.2 m in core MD07-3115, corresponding to the basin-wide high-amplitude reflection present in Unit 5 at about two third of its total thickness (

). Correlation of both tephras is verified by major-element geochemical analysis, showing the same basaltic andesite composition (Fig. 6). They are thus considered to result from the same volcanic eruption. Unfortunately, comparison to the known geochemical composition of major volcanoes and some of the many monogenetic cones in the vicinity of the fjord (D'Orazio et al., 2003; Gutiérrez et al., 2005; Haberle and Lumley, 1998; Kratzmann et al., 2009; Naranjo and Stern, 1998) is not conclusive. The Si-content excludes an origin related to the less evolved (basaltic) monogenetic cones, while the Ti content shows strong affiliations with Hudson eruptions and the K content points to either the Macá, Mentolat, or Cay Volcano.

4.3 Chronology

The correlation of both cores as elaborated in the previous section allows constructing a 'composite' core for which a single, continuous chronology can be established. With this composite core, the older sediments in the fjord as well as the recent sedimentation are covered in great detail (Fig. 7). The model shows two marked changes in sedimentation rate: one at the transition between siliciclastic (Unit 3) and diatom-rich (Unit 4) sedimentation at around 12.3 cal ka BP and another at the onset of Unit 5 around 3.7 cal ka BP. The sedimentation rates in the siliciclastic interval (Unit 3) were markedly higher (~1.7 cm/yr) compared to the diatom-rich interval (Unit 4; ~0.2 cm/yr). The onset of Unit 5 is marked by another abrupt increase in sedimentation rates to ~0.8 cm/yr when considering the sedimentary sequence present in core MD07-3114, while sedimentation rates in core MD07-3115—

located in an area of sediment thinning and characterized by a more condensed Unit 5—decrease to ~0.08 cm/yr (i.e., 3 m of sediment in ~3.7 ka).

The age model additionally allows relating the different tephra layers to well-described volcanic eruptions in the southern Andes, validating the obtained model. The most prominent tephra layer in this part of the fjord is present in Unit 4 (8,130–8,670 cal yrs BP) and shows strong overlap with the age range of one of Hudson Volcano’s major eruption (H1, 7,690–8,720 cal yrs BP Stern and Weller (2012)). As a tephra deposit related to this eruption has also been identified in the inner part of the fjord (Wils et al., 2018), we consider this tephra to result from the H1 eruption (Fig. 7). The tephra layer in Unit 5 (2,150–2,500 cal yrs BP) we interpret to result from Hudson’s T6 eruption (<2,060–2,420 cal yrs BP, Naranjo and Stern (1998)), showing the best age range overlap compared to the Holocene eruptions of volcanoes in the vicinity of the fjord (Fig. 7).

5 Discussion

5.1 Present-day bottom current circulation patterns

Seismic profiling in combination with multibeam bathymetry revealed that the modern seafloor topography in the outer part of Aysén Fjord consists of several local mounded areas and depressions as a result of large lateral thickness variability by sediment concentration during deposition of Unit 5 (, 4). This bathymetric morphology cannot be related to any features on land (Fig. 2) and the sedimentary characteristics of Unit 5 show significantly coarser SS grain sizes compared to the unit below, increasing abruptly at its base. These observations indicate that the boundary between Unit 4 and 5 marks the transition from sedimentation dominated by hemipelagic settling to a current-driven sedimentary environment, resulting in the development of sediment drifts (cf., McCave et al., 1995). The areas of sediment thinning can thus be interpreted as moats, whereas the mounded areas constitute the drift body (Fig. 8A). Core MD07-3115 is thus retrieved at the location of the central moat—where currents are strong and only coarser-grained material can be deposited—while MD07-3114 is located close to the crest of the eastern drift and consists of finer-grained material

accumulating at a rate that is about nine times higher when considering the thickness difference of unit 5 (Fig. 5). The lack of any visible draping hemipelagic sedimentation on either of the seismic profiles in the fjord indicates that drift formation is still ongoing. Likewise, the elongated, erosive channel located just northwest of the coring locations has no recent sedimentation () and is thus also still active to date, likely representing a contourite channel (García et al., 2009; Rebesco et al., 2014). In this way, the identified sediment drifts and channel can provide the first direct information on the present-day bottom current circulation patterns in the southern part of the Patagonian fjords (Fig. 8).

According to Sievers and Silva (2008), the only deep water mass present south of the Meninea sill, and thus in the study area at the conjunction of Aysén Fjord (to the east) and Costa Channel (to the south), is the MSAAW (Fig. 1). Due to the shallowing bathymetry in the southern part of the Costa Channel and south of Casma Island, the inflow of water masses from the Moraleda Channel into Aysén Fjord must occur through the gateway north of Casma Island, where the bathymetry is slightly deeper (Fig. 8). Hence, the Costa Channel is characterized by a roughly southward flow direction formed by the incoming MSAAW. The inflow of MSAAW in Aysén Fjord thus originates from the west, after which it continues southward. As such, the interpreted contourite channel along the coastline of Churrecue Island is considered to transport the incoming water mass eastwards into Aysén Fjord, consistent with the Coriolis effect—considered the driving force to cause bottom currents to stick to slopes (Rebesco et al., 2014)—that results in a current deflection to the left in the Southern Hemisphere. In this way, the contourite channel is likely the result of spilling of the MSAAW over the bathymetric high between Casma and Churrecue Island, forming a ‘plunge pool’ that would explain its erosive nature. In the east of this contourite channel, at least a part of the incoming water mass is deflected southward, towards the Costa Channel. This is likely related to the presence of a bathymetric high north of both core locations, but cannot be verified at this stage due to the lack of high-resolution bathymetry coverage in this area. In any case, this southward deflection resulted in current weakening, so that the contourite

channel gradually evolves into a moat and the formation of the eastern sediment drift in which both cores were retrieved (, Fig. 8A). The southern part of this drift can be identified as fault-controlled (Rebesco et al., 2014), while the northern part is likely formed in between two currents (i.e., the one flowing southward towards the Costa Channel and the other flowing eastward into Aysén Fjord). The western drift constitutes a confined drift (Rebesco et al., 2014), bounded by currents on its eastern and western margin as evidenced by the moats present there. However, the small, individual comma-shaped depressions located in the western extremity of the fjord (Fig. 2) indicate a clear northward current direction. These must thus be formed by a returning MSAAW current, strongly slope-bound in correspondence with the Coriolis effect. It is, however, unclear what controls this outgoing flow direction. This might be related to a circular flow pattern of the MSAAW, in which new MSAAW is continuously flowing into the fjord, then south in the Costa Channel and back north, while it gradually mixes with the overlying water mass at a rate that is in balance with the inflow. Alternatively, the MSAAW in the study area is a relatively stable waterbody that was refilled only sporadically, and internal tides and wind forcing (e.g., Cáceres et al., 2002) combined with the Coriolis effect result in south- and northward bottom currents that stick to the eastern and western slopes, respectively. A third, and most likely, option is a combination of these two processes, in which tides control the inflow of MSAAW and through internal tides most of the currents, but a net clockwise current and gradual mixing with the EW is active as well.

The above interpretation shows that a detailed investigation of the drift-related structures allows linking them with the present-day circulation pattern. However, unravelling how these patterns were established is related to the mechanism behind drift formation, thus requiring thorough insight into the sedimentation and bottom water evolution of the fjord through time.

5.2 Sedimentation history and climate variability

5.2.1 Late Glacial (Units 0–3, ~18–12.3 cal ka BP)

The oldest sedimentation in the outer part of Aysén Fjord (Unit 0, over 30 m thick) is considered to be deposited since ~18 ka, corresponding to the onset of deglaciation in the area (e.g., Davies et al., 2020; Haddam et al., 2018; Kilian and Lamy, 2012). Up until stratigraphic Unit 3, sedimentation is confined by the irregular bedrock topography and restricted to the deepest parts of the outer fjord basin (). Sediments are dominantly siliciclastic with high MS values (Fig. 5), in agreement with the high terrigenous input generally observed during deglaciation (e.g., Hebbeln et al., 2007; Siani et al., 2010). Nevertheless, the mixture of marine, brackish and freshwater diatoms present in Units 2 and 3 (Kissel et al., 2007) suggests that a marine influence was being imposed towards the end of this stratigraphic sequence, consistent with continuously retreating glaciers and a relative sea-level rise. The deepest part of the fjord thus consists of rapid late-glacial sedimentation, reaching values of ~1.7 cm/yr in Unit 3 (Fig. 7) that are likely even higher during deposition of Unit 2 considering the more rapid succession of high-amplitude reflectors (). These are the result of the numerous coarse-grained beds with sharp basal contacts that can thus be interpreted as turbidites. They could be related to glacial lake outburst floods, currently frequently occurring near the Northern Patagonian Icefield (Dussaillant et al., 2009; Vandekerckhove et al., 2020) to which the pre-Holocene setting of Aysén Fjord may have been similar (Davies et al., 2020; García et al., 2018). Continuous recession of these large and thick glaciers in the area thus explains their decreasing frequency from Unit 2 to Unit 3. Alternatively, turbidites could also have a seismic trigger, as postglacial rebound could result in increased activity of one of the numerous LOFZ-related faults in the area or even the megathrust (cf., Beck et al., 1996; Brooks and Adams, 2020; Stewart et al., 2000).

5.2.2 Holocene (Units 4–5, ~12.3 cal ka BP – present)

Since roughly the beginning of the Holocene, sedimentation is less strongly influenced by the input of high-MS glacial sediments but is dominated by fine-grained mud rich in diatoms (Fig. 5). Units 4 and 5

thus represent hemipelagic sedimentation and are post-glacial in age. The entire Aysén Fjord and most likely a large part of its watershed are considered to be deglaciated by 12.3 cal ka BP, consistent with the minimum age of glacial outwash deposits ~15 km inland (Vargas et al., 2013), and with the glacial history of the nearby Cisnes Valley (García et al., 2018). Unit 4 stretches out over the entire outer fjord basin, indicating a relative higher sea level compared to the more confined Unit 3. This is in agreement with the rapid sea-level rise following deglaciation up to ~7 cal ka BP (Garrett et al., 2020; Lambeck et al., 2014; Siddall et al., 2003).

The main difference between Units 4 and 5 resides in their morphology and sedimentation rate rather than their composition. Unit 5 shows the presence of thick sediment drifts whereas Unit 4 is draping and displays significantly lower accumulation rates, at least compared to the mounded areas of Unit 5 (~0.2 compared to 0.8 cm/yr; Fig. 7). Subtle sediment drifts already occur in Unit 4 (Fig. 4), reflecting the increasingly strong marine influence resulting from the (sporadic) inflow of the MSAAW into the fjord basin that only becomes dominant in Unit 5.

Independently of the presence of drifts, the Aysén sediment record displays several intervals with high MS values at 5.5–4.0 cal ka BP and during the last 500 years, superimposed on generally higher MS values after 9.5 cal ka BP (Fig. 9). Since MS is not significantly correlated to sediment grain size ($R = -0.19$, $p > 0.01$), increases in MS along the core likely reflect intervals richer in detrital particles, i.e., increases in terrigenous input by rivers. The progressive increase in MS between 9.5–8.0 cal ka BP is coeval with the main increase in precipitation and westerly wind speed derived from the sediments of Lago Castor (Fiers et al., 2019; Van Daele et al., 2016) (Fig. 9), located in the upper Aysén watershed (Fig. 1A), suggesting that it reflects a gradual increase in precipitation of westerly origin. The latter is coeval with a decrease in SWW speed at 52–53°S and therefore likely reflects an expansion (Lamy et al., 2010) or northward shift (Lamy et al., 2001) of the entire SWW belt. In addition to this long-term shift, the two intervals with the highest MS values (5.5–4.0 cal ka BP and last 500 years) correspond remarkably well to two periods of low Holocene sea surface temperature (SST) in the Concepción

Channel (Fig. 1A), characterized by a strong marine influence (Caniupán et al., 2014) (Fig. 9). Such a relation between decreasing SST and higher detrital input has been observed for the last millennium in two fjords immediately north (Jacaf Fjord; Sepúlveda et al., 2009) and south (Quitalco Fjord; Bertrand et al., 2014) of Aysén Fjord (Fig. 1A, Fig. 9), where it was explained as the response of the SWW belt to changes in temperature. Decreases in temperature result in a stronger polar cell, which in turn displaces the SWW equatorward, resulting in increased year-round precipitation and therefore increased terrestrial input in the Aysén Fjord area (Bertrand et al., 2014). This relation between SST and precipitation is likely also responsible for the increase in detrital input at 5.5–4.0 cal ka BP, which is supported by the 1.5°C decrease in SST at 50°S (Fig. 9) and the darker sediment colour in Aysén Fjord (Fig. 5), likely reflecting increased terrestrial organic matter content. This time interval additionally corresponds to the interval of highest Holocene precipitation (Fiers et al., 2019; Markgraf et al., 2007) and westerly wind speed (Van Daele et al., 2016) in the upper Aysén watershed (Fig. 9). Finally, the more moderate MS increases throughout the Holocene, especially at 8.0–7.5 and 6.2–6.0 cal ka BP, may also represent increased precipitation as they correspond to minor drops in SST (Fig. 9), although these may not be relevant at regional scale. This interpretation of the MS values suggests that the sediments of Aysén Fjord register regional changes in precipitation, like most other fluvially-fed fjords in northern Chilean Patagonia (e.g., Bertrand et al., 2014; Sepúlveda et al., 2009). Based on available datasets, the presence of sediment drifts during the Late Holocene seems to be a unique feature of Aysén Fjord, and can therefore not solely be related to climate variability.

5.2.3 Late Holocene sediment drifts

After an initial increase in SS grain size at the onset of drift formation, variations in SS grain size within the sediment drift suggests that bottom currents gradually weakened during the last 3.7 cal ka BP (Unit 5; Fig. 5 and 9). This weakening trend matches the decrease in westerly wind speed observed in the sediments of Lago Castor (Fiers et al., 2019; Van Daele et al., 2016) (Fig. 9), suggesting a SWW control on MSAAW inflow and bottom current strength in Aysén Fjord. In addition, the decrease in SWW speed during the last 3.7 ka resulted in a direct decrease in precipitation in the Aysén watershed (Fiers et al.,

2019), which in turn led to a thinner EW layer in Aysén Fjord (cf. Silva and Guzmán, 2006) and thus a lower salinity gradient. This generally decreases estuarine circulation patterns (Geyer, 2010), and could thus also contribute to the weakening of bottom water flows. These two mechanisms thus reinforce each other and resulted in a marked decrease in bottom current strength that is reflected in the SS grain size (Fig. 9).

In addition to the general decrease in SS grain size in the sampled sediment drift, the SS grain size also shows a minimum strength around 1.9 cal ka BP (Fig. 5 and 9). This coincides with a period of regionally lower SWW strength and precipitation around 2 cal ka BP as observed in Mallín Pollux (Markgraf et al., 2007) and Lago Shaman (de Porras et al., 2012). This implies that even centennial-scale changes in westerly wind speed modulate the strength of bottom currents in the Patagonian fjords, most likely through decreased MSAAW inflow combined with EW thinning.

5.3 Climatic and tectonic controls on the onset of drift formation

The two major sediment drifts in Aysén Fjord were formed simultaneously around 3.7 cal ka BP. Although bottom currents were likely already present earlier, the drift structures in Unit 4 are much less pronounced (Fig. 4) and sedimentation (rate) was still relatively uniform at both core sites (Fig. 7). This points to a sudden change in bottom current patterns and/or local increase in strength at the transition from Unit 4 to Unit 5, rather than a first appearance of the MSAAW. This is supported by the contourite channel, which must have been formed after or at the end of deposition of Unit 4 to explain the lack of sediment thinning in Unit 4 in that area (

). Moreover, this is consistent with the ACC already extending further north than Chiloé Island since ~9.8 cal ka BP, after which it did not shift any further south (Verleye and Louwye, 2010), so that the SAAW likely already flowed through the Moraleda Channel since the early Holocene.

The onset of drift sedimentation in Aysén Fjord at 3.7 cal ka BP does not seem to reflect a marked change in regional climate conditions. Records around 45°S show the presence of relatively strong SWW during the late Holocene (de Porras et al., 2012; Fiers et al., 2019; Markgraf et al., 2007; Moreno

et al., 2019; Van Daele et al., 2016), but without any specific increase near 3.7 cal ka BP that could explain the onset of sediment drifts. If anything, most regional records concur to indicate that by 3.7 cal ka BP the SWW were well-established in the region (de Porras et al., 2012; Moreno et al., 2019; Quade and Kaplan, 2017) with some records even suggesting a gradual decrease in westerly wind speeds from 4–5 cal ka BP onwards (Fiers et al., 2019; Van Daele et al., 2016). Hence, the abrupt increase in erosion and drift formation does not seem to be related to a change in SWW speed near 45°S. Records located further north (41°S), however, suggest an equatorward expansion of the SWW (Lamy et al., 2010; Lamy et al., 2002) and ACC (Verleye and Louwye, 2010) during the late Holocene, which may have strengthened the Cape Horn current and ultimately resulted in an increase in the inflow of SAAW to the Chilean Fjords through Boca del Guafo (43–44S°), as observed during modern winters (Strub et al., 2019). However, it is hard to imagine that climatic forcing alone would cause such an abrupt start in drift sedimentation and results in the formation of a strongly-erosive contourite channel. Although there is clear relation between climate variability and sedimentation within the drift due to the strong control of SWW speed on ACC inflow, an alternative hypothesis is required to explain the sudden onset of sediment drift formation in Aysén Fjord.

Compilation of paleoseismological research in several locations along the Chilean subduction zone revealed that a major megathrust earthquake occurred roughly along the northern Patagonian fjords (~42–46°S) around 3.9 cal ka BP (Wils et al., 2020). This earthquake triggered a tsunami, of which the imprint in two coastal lakes (Lake Huelde and Lake Cucao) on Chiloé Island was exceptionally large compared to other tsunami deposits (Kempf et al., 2020; Kempf et al., 2017). Moreover, sedimentation in Lake Cucao was significantly altered after this earthquake, which has been attributed to coseismic coastal subsidence (Kempf et al., 2020). The same area subsided about 1 m during the 1960 Great Chilean Earthquake (Plafker and Savage, 1970). Therefore, subsidence during the 3.9 cal ka BP earthquake could have resulted in an abrupt absolute lowering of the Meninea sill or any other blockage, enforcing the precipitation-driven effects on the EW. Tectonic activity could thus have resulted in a sudden increase in MSAAW presence in Aysén Fjord, thus contributing to the present-day

erosion and deposition pattern in the fjord. Nevertheless, further research on the role of the Meninea sill and other topographic heights in the Patagonian channels is required to fully understand the processes that govern bottom current circulation patterns in the area.

6 Conclusions

Thorough analysis of multibeam bathymetry, seismic-reflection data and two radiocarbon-dated ~30 m long piston cores retrieved in the outer part of Aysén Fjord in Chilean Patagonia allowed reconstruction of the late glacial and Holocene sedimentation history of the fjord. This revealed for the first time the presence of active sediment drifts in the Patagonian fjords and channels, providing new insights into the bottom current patterns of northern Patagonia. The oldest sediments in the fjord are siliciclastic and deposited during the late glacial, following the onset of glaciation in the area after ~18 cal ka BP. The subsequent sea-level rise was associated to a period of dominantly marine hemipelagic sedimentation, which is maintained throughout the duration of the Holocene. Most of the sedimentary variability in the fjord can be related to variability in the SWW belt, controlling the amount of terrigenous input into the fjord. Since 3.7 cal ka BP, several large sediment drifts are being formed in the fjord. Their location allowed fine-tuning the previously-established flow patterns in northern Patagonia, showing an incoming as well as a returning flow of the MSAAW. The onset of drift formation is tentatively attributed to the occurrence of a megathrust earthquake, further enhancing the influence of climate on drift formation. This highlights the importance of climatic and tectonic factors on current patterns in the Patagonian fjords and channels and underscores the need for multi-disciplinary studies to understand the evolution of bottom currents through time, especially in complex land-constrained settings.

Data availability

All data necessary to understand the conclusions of this study are presented in the manuscript and/or supplementary info. The studied sediment core halves are stored in the core repository of the Alfred Wegener Institute in Bremerhaven, Germany. Core data (grain size, magnetic susceptibility and

radiocarbon) are publicly available through the PANGAEA data repository:
<https://doi.org/10.1594/PANGAEA.932303>. Seismic profiles are available upon request to the authors.

Acknowledgments

We thank the captain, crew, and scientific party of The International Marine Past Global Change Study R/V Marion Dufresne cruise MD159/PACHIDERME and the DETSUFA survey. Galderic Lastras acknowledges the financial support by a Catalan Government Grups de Recerca Consolidats grant (2017 SGR 315) and the DETSUFA project (CTM2010-09897-E). Katleen Wils recognizes the financial support of the Special Research Fund (BOF) of Ghent University. IHS Kingdom Suite is acknowledged for their educational user license providing seismic interpretation software. We thank two anonymous reviewers and the guest editor (Rachel Brackenridge) for providing constructive comments that improved an earlier version of this manuscript.

References

- Amblas, D., Urgeles, R., Canals, M., Calafat, A.M., Rebesco, M., Camerlenghi, A., Estrada, F., De Batist, M., Hughes-Clarke, J.E., 2006. Relationship between continental rise development and palaeo-ice sheet dynamics, Northern Antarctic Peninsula Pacific margin. *Quaternary Science Reviews* 25, 933-944. <https://doi.org/10.1016/j.quascirev.2005.07.012>.
- Barker, P.F., Thomas, E., 2004. Origin, signature and palaeoclimatic influence of the Antarctic Circumpolar Current. *Earth-Science Reviews* 66, 143-162. <https://doi.org/10.1016/j.earscirev.2003.10.003>.
- Beck, C., Manalt, F., Chapron, E., Rensbergen, P.V., De Batist, M., 1996. Enhanced seismicity in the early post-glacial period: Evidence from the post-würm sediments of lake annecy, northwestern Alps. *Journal of Geodynamics* 22, 155-171. [https://doi.org/10.1016/0264-3707\(96\)00001-4](https://doi.org/10.1016/0264-3707(96)00001-4).
- Bertrand, S., Huguen, K., Sepúlveda, J., Pantoja, S., 2014. Late Holocene covariability of the southern westerlies and sea surface temperature in northern Chilean Patagonia. *Quaternary Science Reviews* 105, 195-208. <https://doi.org/10.1016/j.quascirev.2014.09.021>.
- Bertrand, S., Huguen, K.A., Sepúlveda, J., Pantoja, S., 2012. Geochemistry of surface sediments from the fjords of Northern Chilean Patagonia (44–47°S): Spatial variability and implications for paleoclimate reconstructions. *Geochimica et Cosmochimica Acta* 76, 125-146. <https://doi.org/10.1016/j.gca.2011.10.028>.
- Bianchi, T.S., Arndt, S., Austin, W.E.N., Benn, D.I., Bertrand, S., Cui, X., Faust, J.C., Koziorowska-Makuch, K., Moy, C.M., Savage, C., Smeaton, C., Smith, R., Syvitski, J., 2020. Fjords as Aquatic Critical Zones (ACZs). *Earth-Science Reviews*, 103145. <https://doi.org/10.1016/j.earscirev.2020.103145>.
- Blaauw, M., Christen, J.A., 2011. Flexible paleoclimate age-depth models using an autoregressive gamma process. *Bayesian Analysis* 6, 457-474. <https://doi.org/10.1214/11-ba618>.
- Blott, S.J., Pye, K., 2001. GRADISTAT: a grain size distribution and statistics package for the analysis of unconsolidated sediments. *Earth Surface Processes and Landforms* 26, 1237-1248. <https://doi.org/10.1002/esp.261>.

Brooks, G.R., Adams, J., 2020. A review of evidence of glacially-induced faulting and seismic shaking in eastern Canada. *Quaternary Science Reviews* 228, 106070. <https://doi.org/10.1016/j.quascirev.2019.106070>.

Cáceres, M., Valle-Levinson, A., Sepúlveda, H.H., Holderied, K., 2002. Transverse variability of flow and density in a Chilean fjord. *Continental Shelf Research* 22, 1683-1698. [https://doi.org/10.1016/S0278-4343\(02\)00032-8](https://doi.org/10.1016/S0278-4343(02)00032-8).

Calvete, C., Sobarzo, M., 2011. Quantification of the surface brackish water layer and frontal zones in southern Chilean fjords between Boca del Guafo (43°30'S) and Estero Elefantes (46°30'S). *Continental Shelf Research* 31, 162-171. <https://doi.org/10.1016/j.csr.2010.09.013>.

Caniupán, M., Lamy, F., Lange, C.B., Kaiser, J., Kilian, R., Arz, H.W., León, T., Mollenhauer, G., Sandoval, S., De Pol-Holz, R., Pantoja, S., Wellner, J., Tiedemann, R., 2014. Holocene sea-surface temperature variability in the Chilean fjord region. *Quaternary Research* 82, 342-353. <https://doi.org/10.1016/j.yqres.2014.07.009>.

Carel, M., Siani, G., Delpech, G., 2011. Tephrostratigraphy of a deep-sea sediment sequence off the south Chilean margin: New insight into the Hudson volcanic activity since the last glacial period. *Journal of Volcanology and Geothermal Research* 208, 99-111. <https://doi.org/10.1016/j.jvolgeores.2011.09.011>.

Cembrano, J., Hervé, F., Lavenu, A., 1996. The Liquiñe Ofqui fault zone: a long-lived intra-arc fault system in southern Chile. *Tectonophysics* 259, 55-66. [https://doi.org/10.1016/0040-1951\(95\)00066-6](https://doi.org/10.1016/0040-1951(95)00066-6).

Chen, C.T., Millero, F.J., 1977. Speed of sound in seawater at high pressures. *The Journal of the Acoustical Society of America* 62, 1129-1135. <https://doi.org/10.1121/1.381646>.

D'Orazio, M., Innocenti, F., Manetti, P., Tamponi, M., Tonarini, S., González-Ferrán, O., Lahsen, A., Omarini, R., 2003. The Quaternary calc-alkaline volcanism of the Patagonian Andes close to the Chile triple junction: geochemistry and petrogenesis of volcanic rocks from the Cay and Maca volcanoes (~45°S, Chile). *Journal of South American Earth Sciences* 16, 219-242. [https://doi.org/10.1016/s0895-9811\(03\)00063-4](https://doi.org/10.1016/s0895-9811(03)00063-4).

Davies, B.J., Darvill, C.M., Lovell, H., Bendle, J.M., Dowdeswell, J.A., Fabel, D., García, J.-L., Geiger, A., Glasser, N.F., Gheorghiu, D.M., Harrison, S., Hein, A.S., Kaplan, M.R., Martin, J.R.V., Mendelova, M., Palmer, A., Pelto, M., Rodés, Á., Sagredo, E.A., Smedley, R., Smellie, J.L., Thorndycraft, V.R., 2020. The evolution of the Patagonian Ice Sheet from 35 ka to the present day (PATICE). *Earth-Science Reviews*, 103152. <https://doi.org/10.1016/j.earscirev.2020.103152>.

de Porras, M.E., Maldonado, A., Abarzúa, A.M., Cárdenas, M.L., Francois, J.P., Martel-Cea, A., Stern, C.R., Méndez, C., Reyes, O., 2012. Postglacial vegetation, fire and climate dynamics at Central Chilean Patagonia (Lake Shaman, 44°S). *Quaternary Science Reviews* 50, 71-85. <https://doi.org/10.1016/j.quascirev.2012.06.015>.

Dussailant, A., Benito, G., Buytaert, W., Carling, P., Meier, C., Espinoza, F., 2009. Repeated glacial-lake outburst floods in Patagonia: an increasing hazard? *Natural Hazards* 54, 469-481. <https://doi.org/10.1007/s11069-009-9479-8>.

Fick, S.E., Hijmans, R.J., 2017. WorldClim 2: new 1-km spatial resolution climate surfaces for global land areas. *International Journal of Climatology* 37, 4302-4315. <https://doi.org/10.1002/joc.5086>.

Fiers, G., Bertrand, S., Van Daele, M., Granon, E., Reid, B., Vandoorne, W., De Batist, M., 2019. Hydroclimate variability of northern Chilean Patagonia during the last 20 kyr inferred from the bulk organic geochemistry of Lago Castor sediments (45°S). *Quaternary Science Reviews* 204, 105-118. <https://doi.org/10.1016/j.quascirev.2018.11.015>.

Fisher, R.L., Raitt, R.W., 1962. Topography and structure of the Peru-Chile trench. *Deep Sea Research and Oceanographic Abstracts* 9, 423-443. [https://doi.org/10.1016/0011-7471\(62\)90094-3](https://doi.org/10.1016/0011-7471(62)90094-3).

Fontijn, K., Lachowycz, S.M., Rawson, H., Pyle, D.M., Mather, T.A., Naranjo, J.A., Moreno-Roa, H., 2014. Late Quaternary tephrostratigraphy of southern Chile and Argentina. *Quaternary Science Reviews* 89, 70-84. <https://doi.org/10.1016/j.quascirev.2014.02.007>.

García, J.-L., Maldonado, A., de Porras, M.E., Nuevo Delaunay, A., Reyes, O., Ebensperger, C.A., Binnie, S.A., Lüthgens, C., Méndez, C., 2018. Early deglaciation and paleolake history of Río Cisnes Glacier, Patagonian Ice Sheet (44°S). *Quaternary Research* 91, 194-217. <https://doi.org/10.1017/qua.2018.93>.

610 García, M., Hernández-Molina, F.J., Llave, E., Stow, D.A.V., León, R., Fernández-Puga, M.C., Díaz del Río,
 611 V., Somoza, L., 2009. Contourite erosive features caused by the Mediterranean Outflow Water in the
 612 Gulf of Cadiz: Quaternary tectonic and oceanographic implications. *Marine Geology* 257, 24-40.
 613 <https://doi.org/10.1016/j.margeo.2008.10.009>.
 614 Garreaud, R., Lopez, P., Minvielle, M., Rojas, M., 2013. Large-Scale Control on the Patagonian Climate.
 615 *Journal of Climate* 26, 215-230. <https://doi.org/10.1175/jcli-d-12-00001.1>.
 616 Garrett, E., Melnick, D., Dura, T., Cisternas, M., Ely, L.L., Wesson, R.L., Jara-Muñoz, J., Whitehouse, P.L.,
 617 2020. Holocene relative sea-level change along the tectonically active Chilean coast. *Quaternary*
 618 *Science Reviews* 236, 106281. <https://doi.org/10.1016/j.quascirev.2020.106281>.
 619 GEBCO Compilation Group, 2020. GEBCO 2020 Grid.
 620 Geyer, W.R., 2010. Estuarine salinity structure and circulation, in: Valle-Levinson, A. (Ed.),
 621 *Contemporary Issues in Estuarine Physics*. Cambridge University Press, Cambridge, pp. 12-26.
 622 Gilli, A., Anselmetti, F.S., Ariztegui, D., Beres, M., McKenzie, J.A., Markgraf, V., 2004. Seismic
 623 stratigraphy, buried beach ridges and contourite drifts: the Late Quaternary history of the closed Lago
 624 Cardiel basin, Argentina (49°S). *Sedimentology* 52, 1-23. <https://doi.org/10.1111/j.1365-3091.2004.00677.x>.
 625 Glasser, N.F., Ghiglione, M.C., 2009. Structural, tectonic and glaciological controls on the evolution of
 626 fjord landscapes. *Geomorphology* 105, 291-302. <https://doi.org/10.1016/j.geomorph.2008.10.007>.
 627 Grützner, J., Hillenbrand, C.-D., Rebesco, M., 2005. Terrigenous flux and biogenic silica deposition at
 628 the Antarctic continental rise during the late Miocene to early Pliocene: implications for ice sheet
 629 stability and sea ice coverage. *Global and Planetary Change* 45, 131-149.
 630 <https://doi.org/10.1016/j.gloplacha.2004.09.004>.
 631 Gutiérrez, F., Gioncada, A., González Ferran, O., Lahsen, A., Mazzuoli, R., 2005. The Hudson Volcano
 632 and surrounding monogenetic centres (Chilean Patagonia): An example of volcanism associated with
 633 ridge–trench collision environment. *Journal of Volcanology and Geothermal Research* 145, 207-233.
 634 <https://doi.org/10.1016/j.jvolgeores.2005.01.014>.
 635 Haberle, S.G., Lumley, S.H., 1998. Age and origin of tephras recorded in postglacial lake sediments to
 636 the west of the southern Andes, 44°S to 47°S. *Journal of Volcanology and Geothermal Research* 84,
 637 239-256. [https://doi.org/http://dx.doi.org/10.1016/S0377-0273\(98\)00037-7](https://doi.org/http://dx.doi.org/10.1016/S0377-0273(98)00037-7).
 638 Haddam, N.A., Siani, G., Michel, E., Kaiser, J., Lamy, F., Duchamp-Alphonse, S., Hefter, J., Braconnot, P.,
 639 Dewilde, F., Isgüder, G., Tisnerat-Laborde, N., Thil, F., Durand, N., Kissel, C., 2018. Changes in latitudinal
 640 sea surface temperature gradients along the Southern Chilean margin since the last glacial. *Quaternary*
 641 *Science Reviews* 194, 62-76. <https://doi.org/10.1016/j.quascirev.2018.06.023>.
 642 Hebbeln, D., Lamy, F., Mohtadi, M., Echtler, H., 2007. Tracing the impact of glacial-interglacial climate
 643 variability on erosion of the southern Andes. *Geology* 35, 131-134. <https://doi.org/10.1130/g23243a.1>.
 644 Heirman, K., De Batist, M., Arnaud, F., De Beaulieu, J.-L., 2012. Seismic stratigraphy of the late
 645 Quaternary sedimentary infill of Lac d'Armor (Kerguelen archipelago): a record of glacier retreat,
 646 sedimentary mass wasting and southern Westerly intensification. *Antarctic Science* 24, 608-618.
 647 <https://doi.org/10.1017/s0954102012000466>.
 648 Hogg, A.G., Heaton, T.J., Hua, Q., Palmer, J.G., Turney, C.S.M., Southon, J., Bayliss, A., Blackwell, P.G.,
 649 Boswijk, G., Bronk Ramsey, C., Pearson, C., Petchey, F., Reimer, P., Reimer, R., Wacker, L., 2020.
 650 SHCal20 Southern Hemisphere Calibration, 0–55,000 Years cal BP. *Radiocarbon* 62, 759-778.
 651 <https://doi.org/10.1017/RDC.2020.59>.
 652 Kaiser, J., Lamy, F., Hebbeln, D., 2005. A 70-kyr sea surface temperature record off southern Chile
 653 (Ocean Drilling Program Site 1233). *Paleoceanography* 20, PA4009.
 654 <https://doi.org/10.1029/2005pa001146>.
 655 Kempf, P., Moernaut, J., Van Daele, M., Pino, M., Urrutia, R., De Batist, M., 2020. Paleotsunami record
 656 of the past 4300 years in the complex coastal lake system of Lake Cucao, Chiloé Island, south central
 657 Chile. *Sedimentary Geology* 401, 105644. <https://doi.org/10.1016/j.sedgeo.2020.105644>.
 658 Kempf, P., Moernaut, J., Van Daele, M., Vandoorne, W., Pino, M., Urrutia, R., De Batist, M., 2017.
 659 Coastal lake sediments reveal 5500 years of tsunami history in south central Chile. *Quaternary Science*
 660 *Reviews* 161, 99-116. <https://doi.org/10.1016/j.quascirev.2017.02.018>.
 661

662 Kilian, R., Lamy, F., 2012. A review of Glacial and Holocene paleoclimate records from southernmost
 663 Patagonia (49–55°S). *Quaternary Science Reviews* 53, 1–23.
 664 <https://doi.org/10.1016/j.quascirev.2012.07.017>.
 665 Kissel, C., Leau, H., The Shipboard Scientific party, 2007. MD159-PACHIDERME-IMAGES XV, cruise
 666 report., Les rapports de campagne à la mer. Institut Paul-Emile Victor, p. 105.
 667 Kratzmann, D.J., Carey, S., Scasso, R., Naranjo, J.-A., 2009. Compositional variations and magma mixing
 668 in the 1991 eruptions of Hudson volcano, Chile. *Bulletin of Volcanology* 71.
 669 <https://doi.org/10.1007/s00445-008-0234-x>.
 670 Lambeck, K., Rouby, H., Purcell, A., Sun, Y., Sambridge, M., 2014. Sea level and global ice volumes from
 671 the Last Glacial Maximum to the Holocene. *Proceedings of the National Academy of Sciences* 111,
 672 15296–15303. <https://doi.org/10.1073/pnas.1411762111>.
 673 Lamy, F., Hebbeln, D., Röhl, U., Wefer, G., 2001. Holocene rainfall variability in southern Chile: a marine
 674 record of latitudinal shifts of the Southern Westerlies. *Earth and Planetary Science Letters* 185, 369–
 675 382. [https://doi.org/10.1016/S0012-821X\(00\)00381-2](https://doi.org/10.1016/S0012-821X(00)00381-2).
 676 Lamy, F., Kaiser, J., Ninnemann, U., Hebbeln, D., Arz, H.W., Stoner, J., 2004. Antarctic timing of surface
 677 water changes off Chile and Patagonian Ice Sheet response. *Science* 304, 1959–1962.
 678 <https://doi.org/10.1126/science.1097863>.
 679 Lamy, F., Kilian, R., Arz, H.W., Francois, J.-P., Kaiser, J., Prange, M., Steinke, T., 2010. Holocene changes
 680 in the position and intensity of the southern westerly wind belt. *Nature Geoscience* 3, 695–699.
 681 <https://doi.org/10.1038/ngeo959>.
 682 Lamy, F., Rühlemann, C., Hebbeln, D., Wefer, G., 2002. High- and low-latitude climate control on the
 683 position of the southern Peru-Chile Current during the Holocene. *Paleoceanography* 17, 16–11–16–10.
 684 <https://doi.org/10.1029/2001pa000727>.
 685 Lastras, G., The Shipboard Scientific Party, 2013. DETSUFA Cruise Report. CRG Marine Geosciences,
 686 University of Barcelona (UB), Barcelona, Spain.
 687 Legrand, D., Barrientos, S., Bataille, K., Cembrano, J., Pavez, A., 2011. The fluid-driven tectonic swarm
 688 of Aysen Fjord, Chile (2007) associated with two earthquakes (Mw=6.1 and Mw=6.2) within the
 689 Liquiñe-Ofqui Fault Zone. *Continental Shelf Research* 31, 154–161.
 690 <https://doi.org/10.1016/j.csr.2010.05.008>.
 691 Lobo, F.J., Hernández-Molina, F.J., Bohoyo, F., Galindo-Zaldívar, J., Maldonado, A., Martos, Y.,
 692 Rodríguez-Fernández, J., Somoza, L., Vázquez, J.T., 2011. Furrows in the southern Scan Basin,
 693 Antarctica: interplay between tectonic and oceanographic influences. *Geo-Marine Letters* 31, 451–464.
 694 <https://doi.org/10.1007/s00367-011-0240-4>.
 695 Markgraf, V., Whitlock, C., Haberle, S., 2007. Vegetation and fire history during the last 18,000 cal yr
 696 B.P. in Southern Patagonia: Mallín Pollux, Coyhaique, Province Aisén (45°41'30" S, 71°50'30" W, 640 m
 697 elevation). *Palaeogeography, Palaeoclimatology, Palaeoecology* 254, 492–507.
 698 <https://doi.org/10.1016/j.palaeo.2007.07.008>.
 699 McCave, I.N., Manighetti, B., Robinson, S.G., 1995. Sortable silt and fine sediment size/composition
 700 slicing: Parameters for palaeocurrent speed and palaeoceanography. *Paleoceanography* 10, 593–610.
 701 <https://doi.org/10.1029/94PA03039>.
 702 Moreno, P.I., Francois, J.P., Moy, C.M., Villa-Martínez, R., 2010. Covariability of the Southern
 703 Westerlies and atmospheric CO₂ during the Holocene. *Geology* 38, 727–730.
 704 <https://doi.org/10.1130/g30962.1>.
 705 Moreno, P.I., Simi, E., Villa-Martínez, R.P., Vilanova, I., 2019. Early arboreal colonization, postglacial
 706 resilience of deciduous Nothofagus forests, and the Southern Westerly Wind influence in central-east
 707 Andean Patagonia. *Quaternary Science Reviews* 218, 61–74.
 708 <https://doi.org/10.1016/j.quascirev.2019.06.004>.
 709 Naranjo, J.A., Stern, C.R., 1998. Holocene explosive activity of Hudson Volcano, southern Andes.
 710 *Bulletin of Volcanology* 59, 291–306. <https://doi.org/10.1007/s004450050193>.
 711 Naranjo, J.A., Stern, C.R., 2004. Holocene tephrochronology of the southernmost part (42°30'–45° S) of
 712 the Andean Southern Volcanic Zone. *Revista Geológica de Chile* 31, 224–240.

Palma, S., Silva, N., 2004. Distribution of siphonophores, chaetognaths, euphausiids and oceanographic conditions in the fjords and channels of southern Chile. *Deep Sea Research Part II: Topical Studies in Oceanography* 51, 513-535. <https://doi.org/10.1016/j.dsr2.2004.05.001>.

Plafker, G., Savage, J.C., 1970. Mechanism of the Chilean Earthquakes of May 21 and 22, 1960. *Geological Society of America Bulletin* 81, 1001-1030. [https://doi.org/10.1130/0016-7606\(1970\)81\[1001:motceo\]2.0.co;2](https://doi.org/10.1130/0016-7606(1970)81[1001:motceo]2.0.co;2).

Quade, J., Kaplan, M.R., 2017. Lake-level stratigraphy and geochronology revisited at Lago (Lake) Cardiel, Argentina, and changes in the Southern Hemispheric Westerlies over the last 25 ka. *Quaternary Science Reviews* 177, 173-188. <https://doi.org/10.1016/j.quascirev.2017.10.006>.

Rebesco, M., Hernández-Molina, F.J., Van Rooij, D., Wåhlin, A., 2014. Contourites and associated sediments controlled by deep-water circulation processes: State-of-the-art and future considerations. *Marine Geology* 352, 111-154. <https://doi.org/10.1016/j.margeo.2014.03.011>.

Rintoul, S.R., 2018. The global influence of localized dynamics in the Southern Ocean. *Nature* 558, 209-218. <https://doi.org/10.1038/s41586-018-0182-3>.

Romero, O.E., Kim, J.-H., Hebbeln, D., 2006. Paleoproductivity evolution off central Chile from the Last Glacial Maximum to the Early Holocene. *Quaternary Research* 65, 519-525. <https://doi.org/10.1016/j.yqres.2005.07.003>.

Roque, C., Duarte, H., Terrinha, P., Valadares, V., Noiva, J., Cachão, M., Ferreira, J., Legoinha, P., Zitellini, N., 2012. Pliocene and Quaternary depositional model of the Algarve margin contourite drifts (Gulf of Cadiz, SW Iberia): Seismic architecture, tectonic control and paleoceanographic insights. *Marine Geology* 303-306, 42-62. <https://doi.org/10.1016/j.margeo.2011.11.001>.

Saunders, K.M., Roberts, S.J., Perren, B., Butz, C., Sime, L., Davies, S., Van Nieuwenhuyze, W., Grosjean, M., Hodgson, D.A., 2018. Holocene dynamics of the Southern Hemisphere westerly winds and possible links to CO₂ outgassing. *Nature Geoscience* 11, 650-655. <https://doi.org/10.1038/s41561-018-0186-5>.

Sepúlveda, J., Pantoja, S., Huguen, K.A., Bertrand, S., Figueroa, D., León, T., Drenzek, N.J., Lange, C., 2009. Late Holocene sea-surface temperature and precipitation variability in northern Patagonia, Chile (Jacaf Fjord, 44°S). *Quaternary Research* 72, 400-409. <https://doi.org/10.1016/j.yqres.2009.06.010>.

Sepúlveda, S.A., Serey, A., Lara, M., Pavez, A., Rebolledo, S., 2010. Landslides induced by the April 2007 Aysén Fjord earthquake, Chilean Patagonia. *Landslides* 7, 483-492. <https://doi.org/10.1007/s10346-010-0203-2>.

Serno, S., 2009. Late glacial and Holocene palaeoenvironmental changes in the southern Chilean fjord system: A multi-proxy study of high resolution marine sediment cores, Helmholtz-Zentrum Potsdam – Deutsches GeoForschungsZentrum GFZ. Universität Potsdam, Potsdam.

Siani, G., Colin, C., Michel, E., Carel, M., Richter, T., Kissel, C., Dewilde, F., 2010. Late Glacial to Holocene terrigenous sediment record in the Northern Patagonian margin: Paleoclimate implications. *Palaeogeography, Palaeoclimatology, Palaeoecology* 297, 26-36. <https://doi.org/10.1016/j.palaeo.2010.07.011>.

Siddall, M., Rohling, E.J., Almogi-Labin, A., Hemleben, C., Meischner, D., Schmelzer, I., Smeed, D.A., 2003. Sea-level fluctuations during the last glacial cycle. *Nature* 423, 853-858. <https://doi.org/10.1038/nature01690>.

Sievers, H.A., Silva, N., 2008. Water Masses and Circulation in Austral Chilean Channels and Fjords, in: Silva, N., Palma, S. (Eds.), *Progress in the Oceanographic Knowledge of Chilean Interior Waters, from Puerto Montt to Cape Horn*. Comité Oceanográfico Nacional - Pontificia Universidad Católica de Valparaíso, Valparaíso, pp. 53-58.

Sijp, W.P., England, M.H., 2008. The effect of a northward shift in the southern hemisphere westerlies on the global ocean. *Progress in Oceanography* 79, 1-19. <https://doi.org/10.1016/j.pocean.2008.07.002>.

Silva, N., Guzmán, D., 2006. Physical and chemical characteristics between Boca del Guafo and Aysén Fjord (CIMAR 7 fiordos cruise). *Ciencia y Tecnología del Mar* 29, 25-44.

St-Onge, G., Chapron, E., Mulsow, S., Salas, M., Viel, M., Debret, M., Foucher, A., Mulder, T., Winiarski, T., Desmet, M., Costa, P.J.M., Ghaleb, B., Jaouen, A., Locat, J., 2012. Comparison of earthquake-triggered turbidites from the Saguenay (Eastern Canada) and Reloncavi (Chilean margin) Fjords:

Implications for paleoseismicity and sedimentology. *Sedimentary Geology* 243-244, 89-107.
<https://doi.org/10.1016/j.sedgeo.2011.11.003>.

Stern, C.R., 2004. Active Andean volcanism: its geologic and tectonic setting. *Revista geológica de Chile* 31, 161-206.

Stern, C.R., Weller, D., 2012. A revised Age of 7430±250 14C yrs BP for the Very Large mid-Holocene Explosive H1 Eruption of the Hudson Volcano, Southern Chile, 13th Chilean Geologic Congress, Antofagasta, Chile, p. 2.

Stewart, I.S., Sauber, J., Rose, J., 2000. Glacio-seismotectonics: ice sheets, crustal deformation and seismicity. *Quaternary Science Reviews* 19, 1367-1389. [https://doi.org/10.1016/S0277-3791\(00\)00094-9](https://doi.org/10.1016/S0277-3791(00)00094-9).

Strub, P.T., James, C., Montecino, V., Rutllant, J.A., Blanco, J.L., 2019. Ocean circulation along the southern Chile transition region (38° -46°S): Mean, seasonal and interannual variability, with a focus on 2014-2016. *Prog Oceanogr* 172, 159-198. <https://doi.org/10.1016/j.pocean.2019.01.004>.

Strub, P.T., Mesias, J.M., Montecino, V., Rutllant, J., Salinas, S., 1998. Coastal ocean circulation off western South America. John Wiley, New York.

Syvitski, J.P., Burrell, D.C., Skei, J.M., 1987. Fjords: processes and products. Springer Science & Business Media, Berlin, Germany.

Van Daele, M., Bertrand, S., Meyer, I., Moernaut, J., Vandoorne, W., Siani, G., Tanghe, N., Ghazoui, Z., Pino, M., Urrutia, R., De Batist, M., 2016. Late Quaternary evolution of Lago Castor (Chile, 45.6°S): Timing of the deglaciation in northern Patagonia and evolution of the southern westerlies during the last 17 kyr. *Quaternary Science Reviews* 133, 130-146. <https://doi.org/10.1016/j.quascirev.2015.12.021>.

Vandekerckhove, E., Bertrand, S., Mauquoy, D., McWethy, D., Reid, B., Stammen, S., Saunders, K.M., Torrejón, F., 2020. Neoglacial increase in high-magnitude glacial lake outburst flood frequency, upper Baker River, Chilean Patagonia (47°S). *Quaternary Science Reviews* 248, 106572. <https://doi.org/10.1016/j.quascirev.2020.106572>.

Vargas, G., Rebolledo, S., Sepúlveda, S.A., Lahsen, A., Thiele, R., Townley, B., Padilla, C., Rauld, R., Herrera, M.J., Lara, M., 2013. Submarine earthquake rupture, active faulting and volcanism along the major Liquiñe-Ofqui Fault Zone and implications for seismic hazard assessment in the Patagonian Andes. *Andean Geology* 40. <https://doi.org/10.5027/andgeoV40n1-a07>.

Verleye, T.J., Louwye, S., 2010. Late Quaternary environmental changes and latitudinal shifts of the Antarctic Circumpolar Current as recorded by dinoflagellate cysts from offshore Chile (41°S). *Quaternary Science Reviews* 29, 1025-1039. <https://doi.org/10.1016/j.quascirev.2010.01.009>.

Villa-Martínez, R., Moreno, P.I., 2007. Pollen evidence for variations in the southern margin of the westerly winds in SW Patagonia over the last 12,600 years. *Quaternary Research* 68, 400-409. <https://doi.org/10.1016/j.yqres.2007.07.003>.

Wils, K., Van Daele, M., Kissel, C., Moernaut, J., Schmidt, S., Siani, G., Lastras, G., 2020. Seismo-turbidites in Aysén Fjord (southern Chile) reveal a complex pattern of rupture modes along the 1960 megathrust earthquake segment. *Journal of Geophysical Research: Solid Earth* 125, e2020JB019405. <https://doi.org/10.1029/2020JB019405>.

Wils, K., Van Daele, M., Lastras, G., Kissel, C., Lamy, F., Siani, G., 2018. Holocene event record of Aysén Fjord (Chilean Patagonia): An interplay of volcanic eruptions and crustal and megathrust earthquakes. *Journal of Geophysical Research: Solid Earth* 123, 324-343. <https://doi.org/10.1002/2017JB014573>.

Figure captions

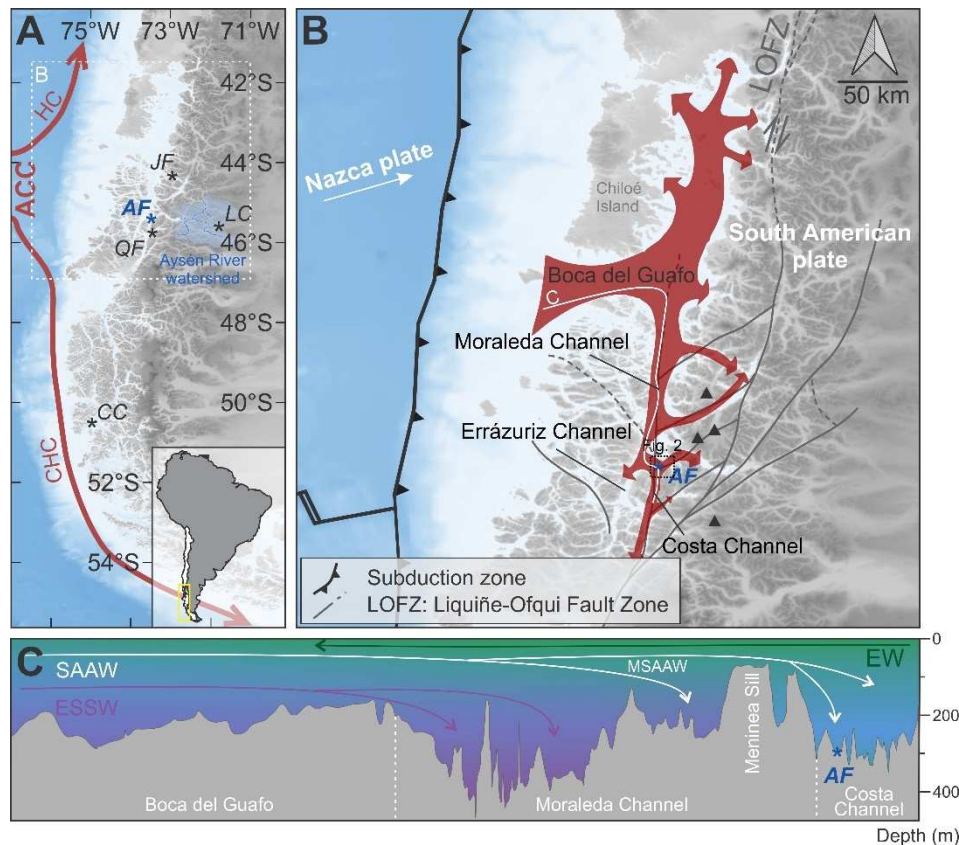


Fig. 1: Tectonic and oceanographic setting of Aysén Fjord (AF), located in southern Chile. A) The regional oceanic circulation pattern is dominated by the Antarctic Circumpolar Current (ACC). The latter hits the continent between about 40-45°S, where it splits into the northward Humboldt Current (HC) and the southward Cape Horn Current (CHC). Additional sites used in this study are indicated: JF = Jacaf Fjord, LC = Lago Castor, QF = Quitrailco Fjord and CC = Concepción Channel. B) Close-up on the study area, with indication of the approximate trace of the Chilean subduction zone, where the Nazca plate subducts beneath the South American plate. The trench-parallel component of oblique subduction is accommodated by the presence of the Liqueñe-Ofqui Fault Zone (LOFZ), of which several fault branches intersect Aysén Fjord. The four main volcanoes in the vicinity of Aysén Fjord are indicated by black triangles (from north to south: Mentolat, Cay, Macá, and Hudson Volcano). The circulation pattern in the Patagonian fjords is indicated in red. The latter enters the fjords through the Boca del Guafo where it is split into two branches. The southern branch enters the Moraleda channel, continuing southwards through the Errázuriz and Costa Channel, the latter passing by Aysén Fjord (Sievers and Silva, 2008). C) Cross-section showing the bathymetry (GEBCO Compilation Group, 2020)

and the different water masses in the region following the white line in panel B (Sievers and Silva, 2008): ESSW = Equatorial Subsurface Water (purple), (M)SAAW = (Modified) Subantarctic Water (blue) and EW = estuarine water (green). Continued southward flow of the ESSW is blocked by the presence of the Meninea sill.

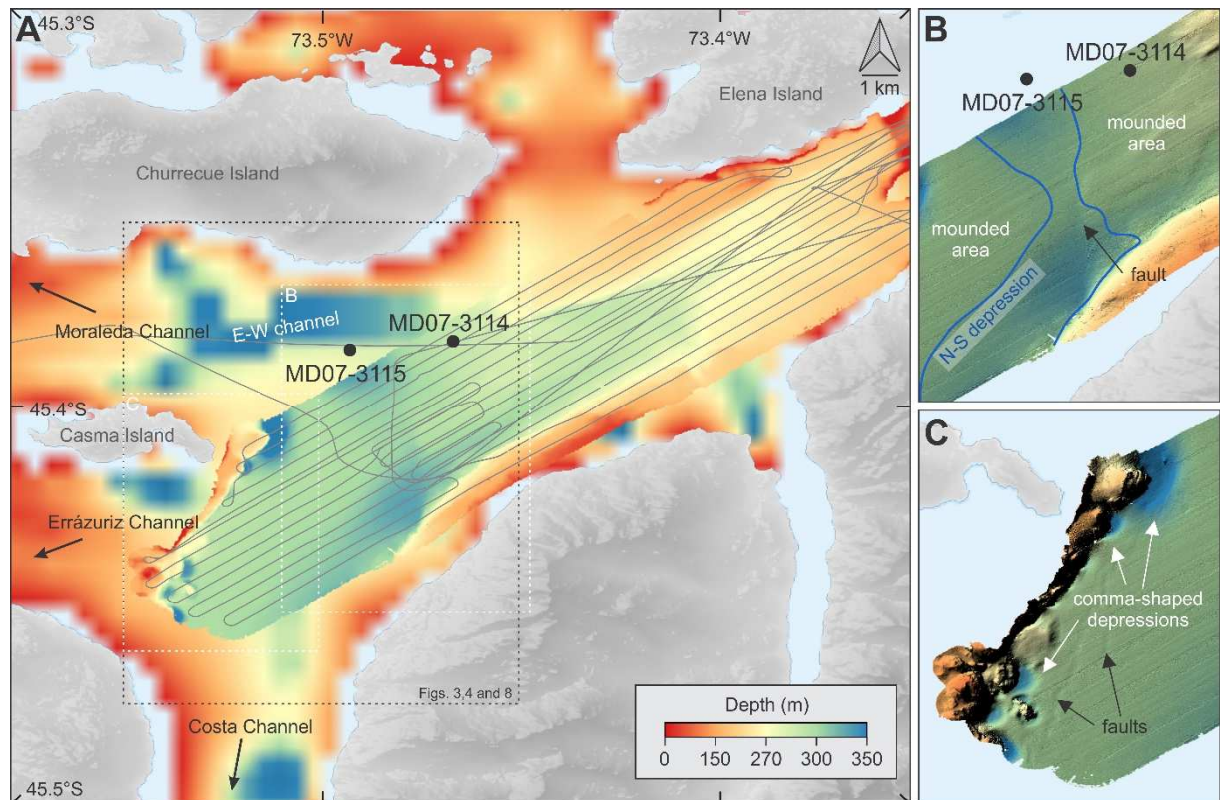


Fig. 2: Bathymetric setting of the study area. A) Multibeam bathymetric map of the outer part of Aysén Fjord plotted on a GEBCO bathymetry map (GEBCO Compilation Group, 2020), showing the TOPAS seismic lines (grey) and the two core locations (black dots, MD07-3114 and MD07-3115). The apparent offset in water depth between both bathymetric maps is mainly the result of a resolution difference. A major east-west oriented channel is present just north of both core locations. Detailed visualization of other relevant features visible on the multibeam bathymetry are presented in panels B and C, with hill shading. B) A north-south oriented elongated depression is located at the longitude of core location MD07-3115, in between two mounded areas. A fault trace can be identified on the eastern side of this depression. C) Several small, individual depressions with a comma-like shape can be observed in the western extremity of the fjord, near Casma Island. Surficial fault traces can also be identified.

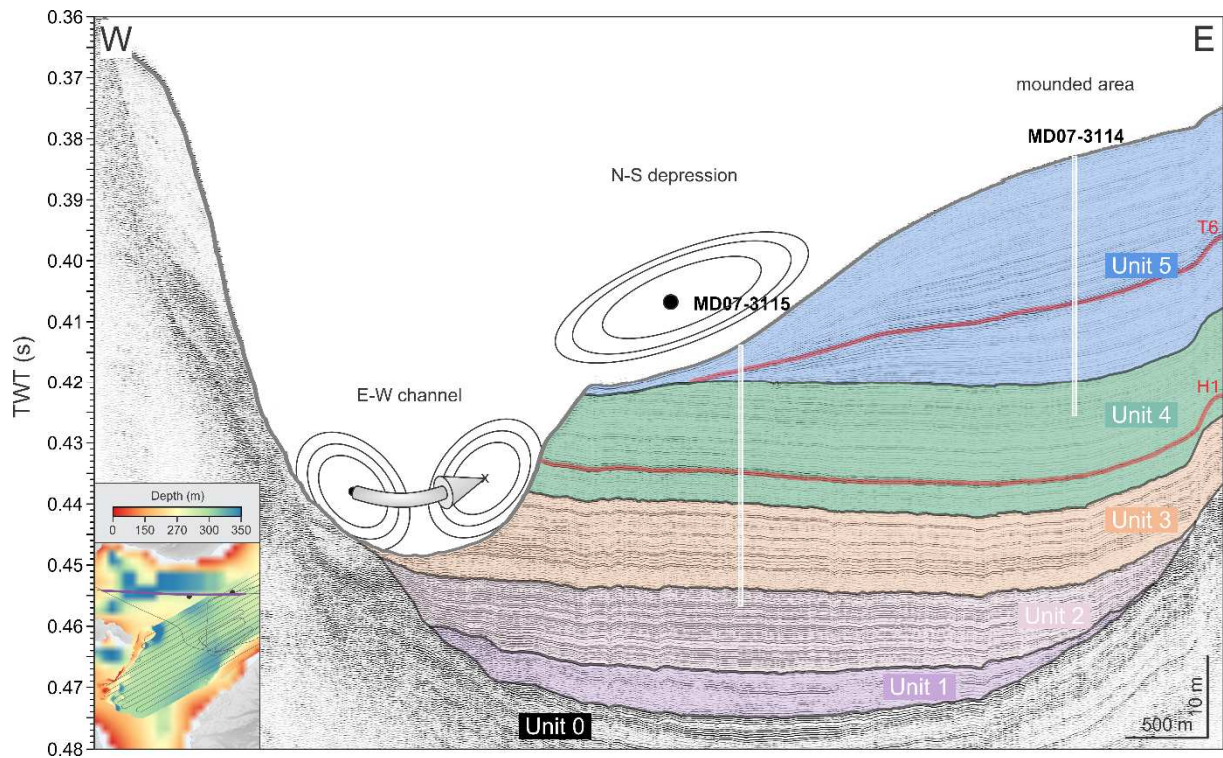


Fig. 3: Interpreted TOPAS seismic profile 209_002 (vertical exaggeration 50 times), expressed in two-way travel time (TWT), with indication of the interpreted current direction at multiple locations. Note that these all represent the same current, flowing quasi-parallel to the profile orientation in the erosive E-W channel (illustrated by the arrow) and (partially) deflecting southward at the location of MD07-3115. A projected length for both sediment cores assuming an acoustic velocity of 1,500 m/s (Chen and Millero, 1977) is indicated. The location of the profile (purple line) and cores (black dots) with respect to the fjord is given in the lower left corner (see Fig. 2). Six seismic-stratigraphic units can be defined (Unit 0-5) and are indicated by colour-coding. The two tephra layers (T6 and H1) are indicated in red. An uninterpreted version of this profile can be found in supplementary info (Fig. S1).

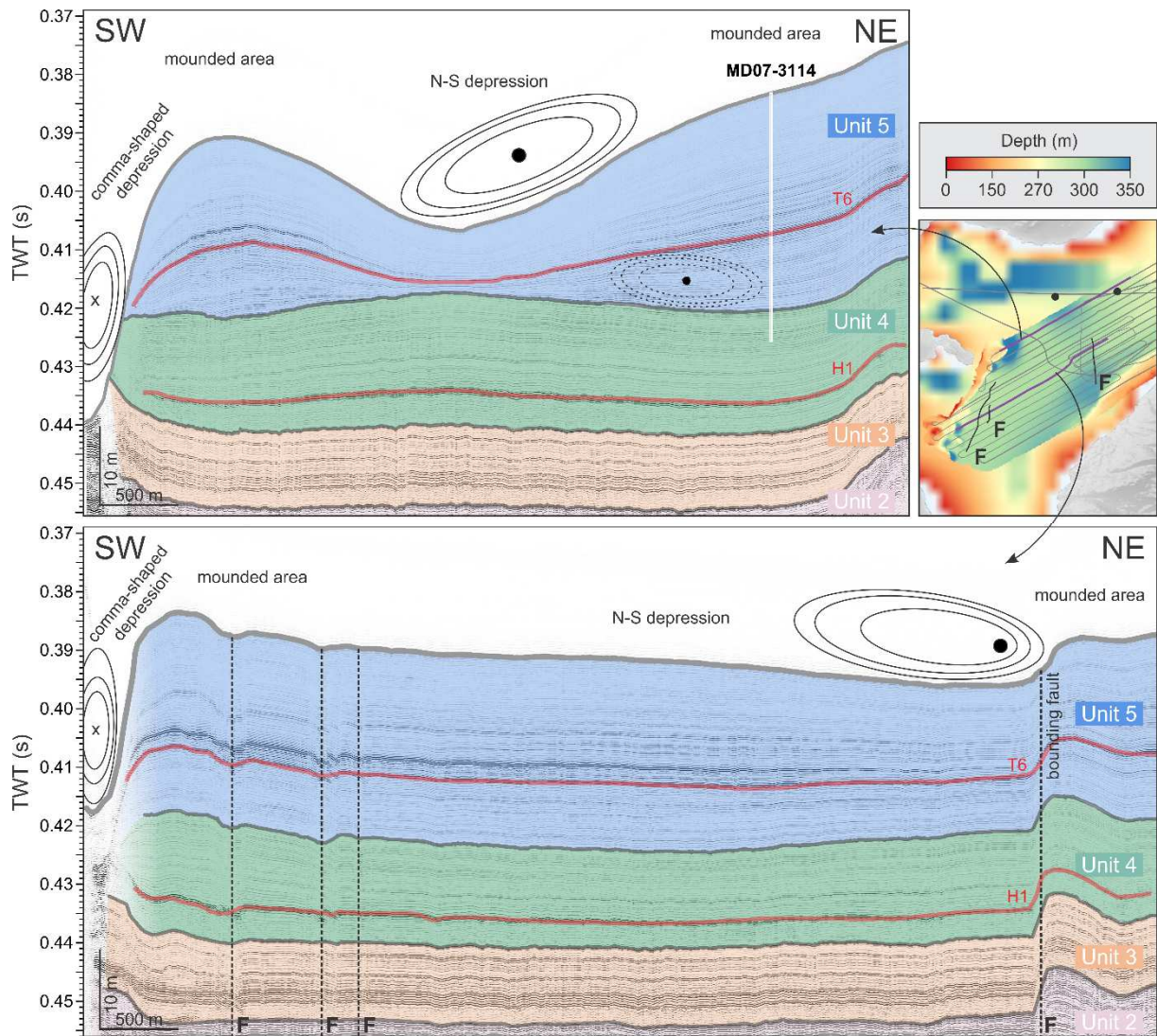


Fig. 4: Interpreted TOPAS seismic profiles 187 (upper panel) and 173 (lower panel) (vertical exaggeration 50 times), expressed in two-way travel time (TWT), with indication of the inferred current directions (dashed when less certain). A projected length for core MD07-3114 assuming an acoustic velocity of 1,500 m/s (Chen and Millero, 1977) is indicated in the upper profile. The location of both profiles (purple lines) and cores (black dots) with respect to the fjord is given in the upper right corner (see Fig. 2). Seismic-stratigraphic Units 2-5 are indicated by colour-coding, similar to those used in . Faults (F) are indicated in black on the profiles (dashed lines) and on the bathymetry (full lines). The two tephra layers (T6 and H1) are indicated in red. An uninterpreted version of these profiles can be found in supplementary info (Fig. S2).

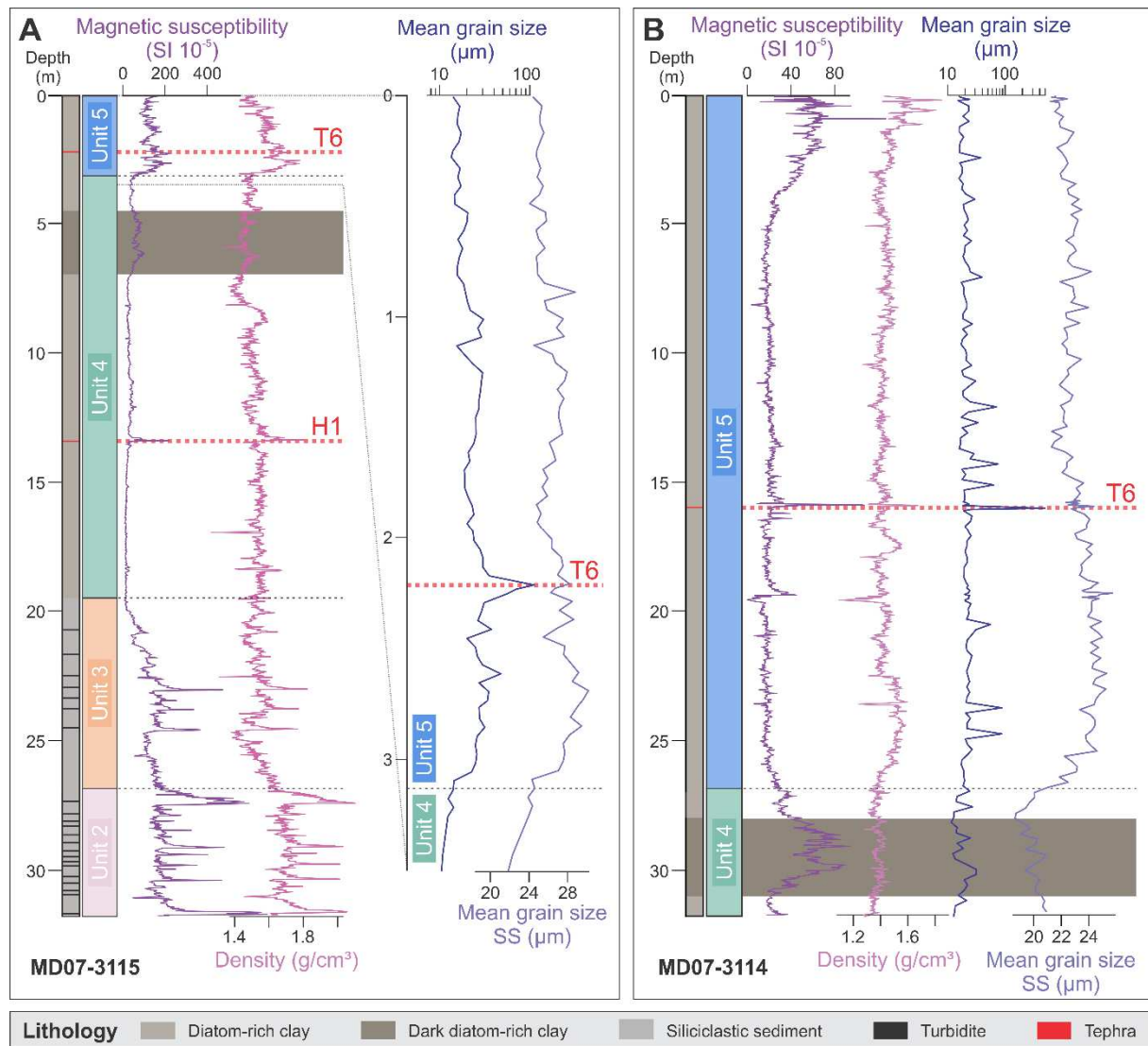
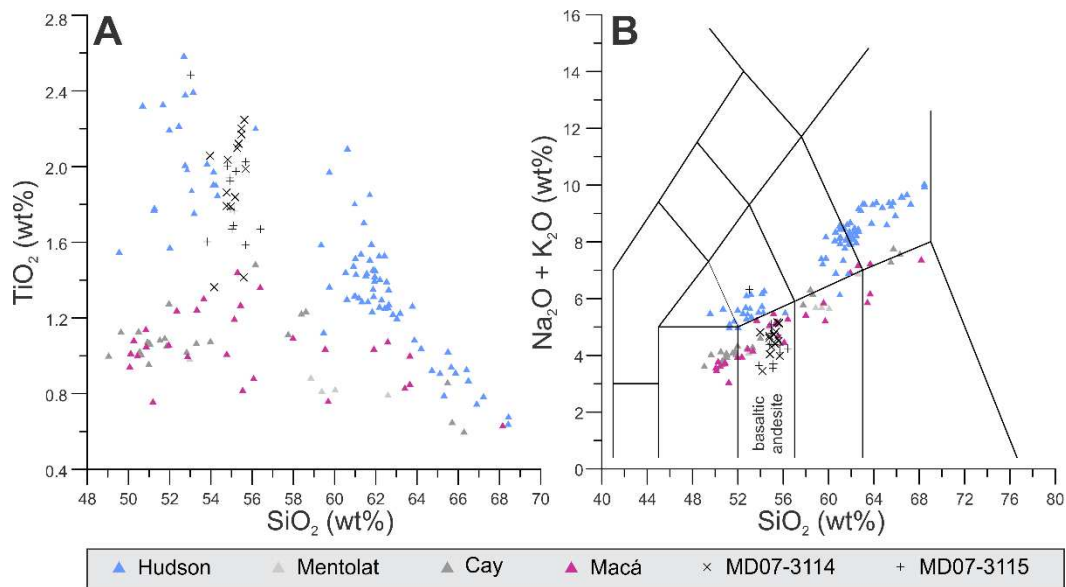


Fig. 5: Sedimentological characteristics of core MD07-3115 (A) and MD07-3114 (B). The sedimentary characteristics are indicated by a schematic lithology representation (diatom-rich clays in brown, siliciclastic sediment in grey, turbidites in black, tephra in red), presented along-side the magnetic susceptibility (purple), density (pink), mean grain size (dark blue), and sortable silts (SS, light blue) values. For core MD07-3115, only the grain-size results for the upper 3.5 m of sediment are presented. The darker-coloured sediment interval within Unit 4, marked by two peaks in magnetic susceptibility and present in both cores, is indicated in dark grey. The sedimentological variability in both cores can be related to seismic-stratigraphic Units 2 to 5, indicated by colour-coding according to . The two tephra layers (T6 and H1) are indicated in red.



869

870 Fig. 6: Major-element concentrations of glass shards in a tephra layer (T6) present in both cores. Both
 871 show a very similar composition, and are considered to result from the same eruption. Comparison to
 872 whole-rock composition of Mentolat, Cay, Macá, and Hudson volcanoes and volcanic glass of Hudson
 873 Volcano (D'Orazio et al., 2003; Gutiérrez et al., 2005; Haberle and Lumley, 1998; Kratzmann et al., 2009;
 874 Naranjo and Stern, 1998) shows that the Ti-content of this tephra layer (A) points to a Hudson Volcano
 875 origin, while the total alkali content (B) advocates for an eruption of any of the other volcanoes. The
 876 Si-content excludes an origin related to any of the less evolved monogenetic cones in the vicinity of
 877 the fjord.

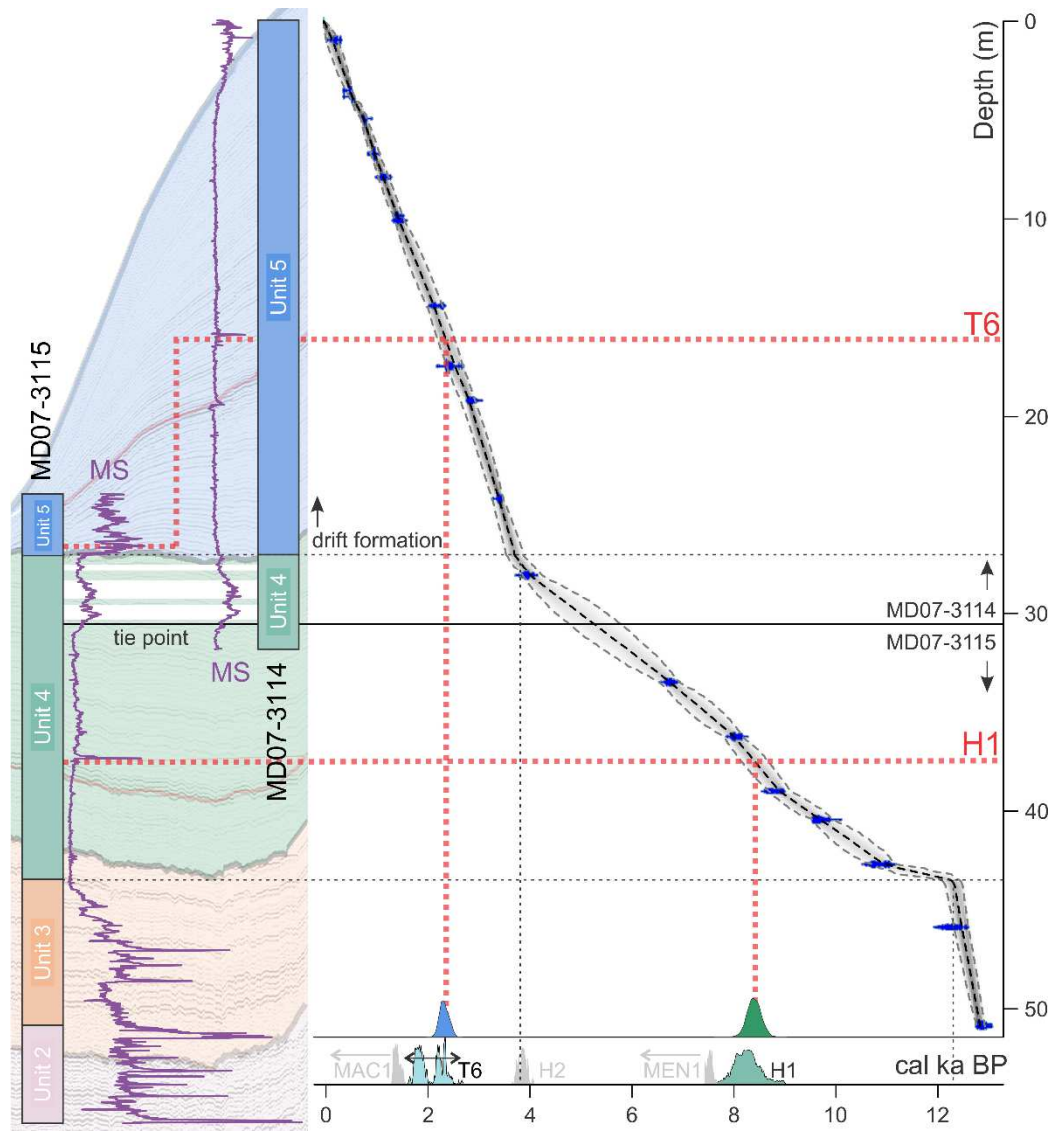


Fig. 7: Age-depth model obtained for the 'composite' core, covering the sediment drift as well as the older sedimentation in the fjord. Left: core-to-core correlation, pinpointed by three simultaneous increases (white beams) in magnetic susceptibility (MS) values (purple). The tie point in Unit 4 used to construct the composite core is indicated. Both cores are schematically represented by their sedimentary units, which are correlated to the seismic units as shown by seismic line 209_002 in the background (colour-coded according to). Right: age model (95% confidence interval in grey) for both sediment cores constructed using calibrated radiocarbon ages (blue). Two changes in sedimentation rate can be observed (dashed lines): at the boundary between Unit 3 and 4 and between Unit 4 and 5, the latter corresponding to the onset

of drift formation. The age range of two tephra layers (T6 and H1, red) in the cores (blue and green) are indicated and compared to the ages of volcanic eruptions (bottom axis) described in literature (Haberle and Lumley, 1998; Naranjo and Stern, 1998, 2004; Stern and Weller, 2012).

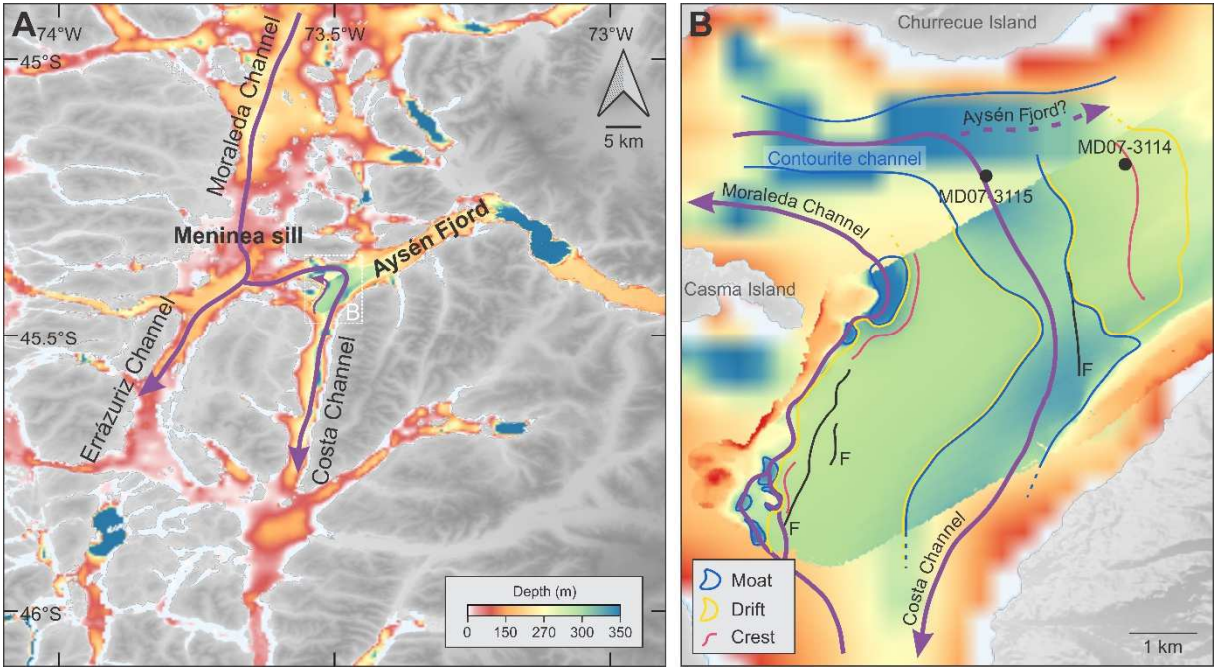


Fig. 8: Present-day current patterns of the (M)SAAW in the Patagonian fjords (purple). A) Visualization of the current patterns in the surroundings of Aysén Fjord, derived from our seismic and bathymetrical data in combination with the flow pattern suggested by Sievers and Silva (2008) indicated on a GEBCO bathymetric map (GEBCO Compilation Group, 2020). B) Bathymetric map of the outer part of Aysén Fjord (see Fig. 2) with indication of sediment drifts (moats in blue, drifts in white, drift crest in yellow) and the contourite channel, showing a detailed pattern of inflowing and outflowing MSAAW. Faults are indicated in black (F).

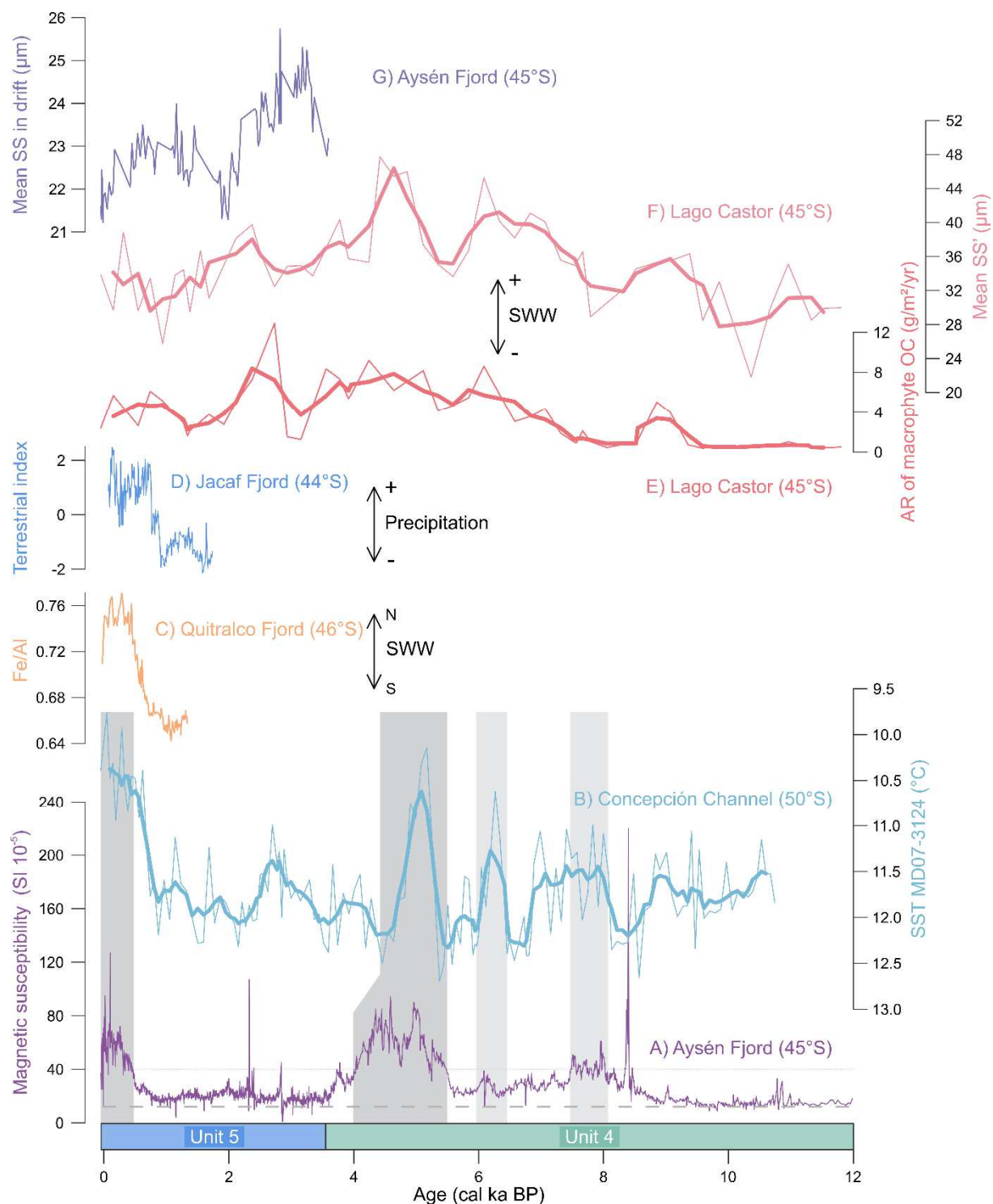


Fig. 9: Comparison of sedimentological data for the composite core in Aysén Fjord with regional records of sea surface temperature (SST), Southern Westerly Wind (SWW) strength and/or latitudinal position and precipitation. From bottom to top: A) magnetic susceptibility in Aysén Fjord (composite core, this study), B) alkenone-based SST in Canal Concepción (Caniupán et al., 2014), C) ICP-OES-based Fe/Al counts in Quitralco Fjord (Bertrand et al., 2014), D) terrestrial index (PCA score) based on bulk

905 organic geochemistry in Jacaf Fjord (Sepúlveda et al., 2009), E) accumulation rate (AR) of macrophyte
906 organic carbon (OC) in Lago Castor (Fiers et al., 2019), F) mean modified (10-125 μm) sortable silt (SS')
907 in Lago Castor (Van Daele et al., 2016), and G) mean sortable silt (SS) grain size in Aysén Fjord
908 (composite core, this study, see Fig. 1A for locations). The extent of Units 4 and 5 are indicated, of
909 which the transition is marked by the onset of sediment drift formation.

910 **Table captions**

911 Table 1: Overview of all radiocarbon ages with their depth in the MD07-3114 and MD07-3115 cores as well as the composite depth used for age-depth
 912 modelling derived from correlation of both cores. All ages were calibrated using the SHCal20 calibration curve (Hogg et al., 2020). The reservoir age of the
 913 marine samples is estimated at 550 years (Serno, 2009), to which we add an uncertainty of 40 years.

Core ID	Sample Number	Depth (cm)	Composite depth (cm)	Material	14C age (years BP)	2σ calibrated age (years BP)	Relative probability (%)	Reservoir age (years)
MD07-3114	1	95	95	leaf fragments	215 ± 30	0-24	4.4	
						72-83	2	
						101-113	2.2	
						139-229	62.9	
						242-298	23.4	
	2	351	351	leaf fragments	420 ± 30	327-380	31.3	
						385-403	4.3	
						439-501	59.4	
	3	382	382	scaphopods	1040 ± 25	804-867	41.3	550 ± 40
						900-936	39.7	
						940-957	13.9	
	4	493	493	leaf fragments	895 ± 30	682-705	7.7	
						718-799	84.2	
						871-879	1.9	
						891-896	1	
	5	671	671	leaf fragments	1070 ± 35	805-866	17.3	
						901-980	73.8	
						1029-1047	3.9	

	6	789	789	bivalve	1810 ± 35	1586-1747 1773-1784 1797-1810	91.1 1.8 2	550 ± 40
	7	984	984	leaf fragments	1550 ± 35	1312-1431 1437-1480 1498-1511	82.4 10.1 2.5	
	8	1008	1008	scaphopods	2120 ± 45	1928-1971 1986-2137 2272-2291	11 81.3 2.7	550 ± 40
	9	1440	1440	bivalve	2760 ± 30	2755-2881 2905-2919	92.6 2.3	550 ± 40
	10	1745	1745	leaf fragments	2410 ± 35	2181-2195 2209-2223 2320-2503 2505-2513 2593-2613 2639-2695	1.3 0.9 81.3 0.5 3.4 7.7	
	11	1919	1919	leaf fragments	2790 ± 55	2754-2968 2979-2995	93 1.9	
	12	2416	2416	leaf fragments	3220 ± 35	3267-3287 3335-3456 3473-3480	3.5 90.3 1.2	
	13	2808	2808	bivalve	4210 ± 30	4579-4603 4605-4605 4610-4834	5.3 0.2 89.5	550 ± 40
	14	940	3349	bivalve	6510 ± 35	7280-7299 7306-7431 7449-7467	2.6 89.4 2.8	550 ± 40
MD07-3115								

	15	1216	3625	bivalve	7810 ± 55	8412-8649 8672-8696	93.2 1.8	550 ± 40
	16	1492	3901	bivalve	8520 ± 40	9437-9539	95	550 ± 40
	17	1636	4045	bivalve	9300 ± 40	10282-10571	95	550 ± 40
	18	1862	4271	bivalve	10105 ± 50	11322-11599 11601-11779 11800-11834	49.2 42 3.8	550 ± 40
	19	2180	4589	scaphopods	11000 ± 50	12765-18978 12986-13013 13038-13065	87.6 3.6 3.7	550 ± 40
	20	2672	5081	wood	11000 ± 40	12766-12975 12991-13000 13042-13052	93 0.9 1	
	21	2683	5092	wood	11008 ± 50	12768-12979 12984-73017 13038-13067	84.7 5.4 4.9	

914